

Laboratory Astrophysics:
Spectral Analysis of Photoionized Neon

James MacArthur
Advisor: David Cohen

March 14, 2011

Abstract

A curve of growth analysis was applied to photoionized neon absorption spectra from gas cell experiments at Sandia National Laboratory's Z facility. The gas cell experiments, designed to photoionize neon up to helium and hydrogen-like species, produce a photoionized plasma comparable to astrophysical plasmas measured in high mass X-ray binaries or Seyfert 2 galaxies. A proper characterization of the photoionized plasma in the gas cell can be used to benchmark photoionization codes like Cloudy and XSTAR used by the astrophysics community. The curve of growth analysis of absorption spectra from neon was applied to calculate the charge state distribution of the neon. The analysis, performed using a Voigt line-profile with the $1s^2 \rightarrow 1snp$ line series on Ne IX, shows that additional line broadening mechanisms are present. A preliminary analysis of additional line broadening from the Stark effect was also performed.

Contents

1	Introduction	3
1.1	Plasmas: Collisional or Photoionized	4
1.2	The Importance of Photoionized Plasmas	6
1.2.1	High Mass X-ray Binaries	7
1.2.2	Seyfert Galaxies	8
1.3	Experimental Verification	9
1.4	The Z Machine	10
1.5	Gas Cell Experiments	11
1.6	Statement of Purpose	12
2	Computer Modeling	14
2.1	VISRAD	14
2.2	PrismSPECT	16
2.3	Actual Measurements	18
3	Curve of Growth Analysis	22
3.1	Equivalent Width	23
3.2	Optical Depth	24
3.3	Line-profile Functions	25
3.3.1	The Lorentzian Profile	26
3.3.2	The Gaussian Profile: Doppler Broadening	29
3.3.3	The Voigt Profile	30
3.3.4	Zeeman Splitting	31
3.3.5	Stark Broadening	32
3.4	An Example Curve of Growth	34
4	Spectral Analysis and Discussion	38
4.1	Equivalent Width Measurement	38
4.2	Comparing Experimental and Theoretical COG	42
4.3	Conclusion	46
5	Acknowledgements	47

Chapter 1

Introduction

Plasmas pervade astrophysical environments; stars, supernovae, black hole accretion disks, and even the interstellar medium are primarily composed of plasma. To understand the processes governing these objects and the universe as a whole, the tools and methods of analysis must be accurate.

Accurate atomic data, like the ionization energies for neon shown in Figure 1.1, is important. Atomic data can be calculated theoretically, but it is also important to experimentally verify the results.

The models that are used to analyze these objects also need verification; thorough benchmarking of the relevant code is critical to the model's viability. A reliable way of benchmarking an astrophysical model is to apply it to a controlled situation in a laboratory. It is not always trivial to do this, however. To benchmark a model describing Ne IX ionized by photons, a laboratory would need a strong source of X-rays. Subsequent chapters are spent on this problem. The Z machine at Sandia National Laboratory can direct hard X-rays at neon, but the ionized neon must be properly characterized before any code benchmarking is attempted.

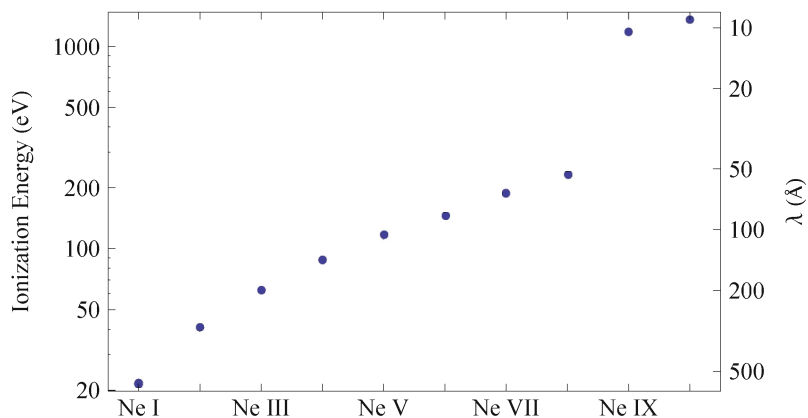
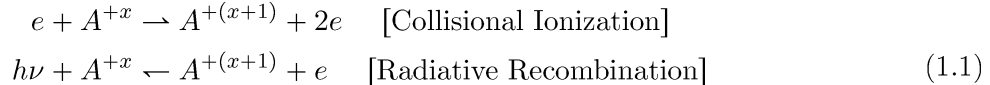


Figure 1.1: Approximate ionization energies for neon atoms in the ground state [1]. The large jump in ionization energy occurs because the electrons in Ne IX and Ne X must be ionized from the $1s$ level. The increasing trend towards higher ionization energies is a consequence of shielding electrons being removed.

1.1 Plasmas: Collisional or Photoionized

One way to categorize plasmas is based on the dominant ionization mechanism. In the aptly named collisionally ionized plasma, collisions between atoms containing bound electrons and other particles (usually free electrons, though collisions with other atoms or ions occur) liberate electrons from the atoms. If A^{+x} represents an atom of species A ionized x times and e represents an electron, collisional ionization is characterized by the relation



The arrows indicate the typical reaction direction; the balance between collisional ionization and radiative recombination dictates the ionization balance. This type of ionization is dominant in dense, high temperature plasmas, since collisional ionization is a two body process (and therefore depends on the product of the ion and electron densities) and a larger electron velocity increases the energy and collisional frequency.

Collisionally ionized plasmas are common in the earth and throughout the universe. Planetary cores, stars, stellar coronae, and black hole accretion disks are just a few examples. Spectroscopic diagnostics can determine the plasma parameters, which can in turn inform scientists about the physics behind the observations. Stellar corona, for example, are well modeled by codes for hot optically thin plasmas like APEC [2], a popular model in the astrophysics community. Since the densities and temperatures required for a collisionally ionized plasma are attainable in the laboratory (the Swarthmore Spheromak Experiment (SSX) can attain coronal plasma conditions), codes like APEC and the atomic parameters they require have been well benchmarked by laboratory experiment [3].

The other ionizing process is photoionization. As the name suggests, energetic photons incident on an atom deposit their energy by ejecting an electron from its potential well in photoionized plasmas. As Figure 1.1 demonstrates, ejecting an electron from neon in its ground state takes at least extreme ultraviolet radiation.¹ Photoionization is balanced by radiative recombination in a photoionized plasma,



where the energy of the photon $h\nu$ must exceed the ionization energy. The rate of ionization is only proportional to one factor of density (the ion density); the incident photons can be translated into a flux. The condition for ionization equilibrium is then [4, 5]

$$n_{A^{+x}} \int_{\nu^*}^{\infty} \sigma_{PI} \mathcal{N}_{\nu} d\nu = n_{A^{+(x+1)}} n_e \int_0^{\infty} \sigma_R f_v v dv \quad \text{[Photoionized]} \quad (1.3)$$

where $n_{A^{+x}}$ and n_e are the number of atoms of species A^{+x} and electrons per unit volume, $h\nu^*$ is the ionization potential for that ion, σ_{PI} is the photoionization cross section of A^{+x} , \mathcal{N}_{ν} is the number of photons with frequency ν entering a unit area per second (Flux/ $h\nu$), and σ_R and f_v are the recombination cross-section and velocity distribution as a function of the electron velocity,

¹Neon has an atypically large first ionization energy because fills the L shell in its ground state exactly; it is a noble gas. Most neutral atoms have ionization energies between 5 and 10 eV.

ν (see Table 1.1 for reference). Each side represents the number of photoionizations (left) or recombinations (right) per second in a unit volume.

There are three important facts about photoionized plasmas hidden in Equation (1.3). The first was previously addressed - in order to have a photoionized plasma, there must be energetic photons available for absorption. Starting integration at the frequency ν^* only counts photons with enough energy to eject an electron. If not enough high energy radiation is available the plasma will not be photoionized. To ionize an atom like neon up to Ne IX or Ne X, a strong X-ray source is required.

Equation (1.3) also contains important information about the density of a photoionized plasma. The volumetric photoionization rate is only proportional to one factor of density, $n_{A^{+x}}$. Compare that with the volumetric collisional ionization rate which is proportional to the density squared, $n_e n_{A^{+x}}$ (just like radiative recombination). For comparison with Equation (1.3), the ionization equilibrium equation in a collisionally ionized plasma is [6]

$$n_{A^{+x}} n_e \int_0^\infty \sigma_{CI} f_v \nu dv = n_{A^{+(x+1)}} n_e \int_0^\infty \sigma_R f_v \nu dv \quad [\text{Collisionally Ionized}] \quad (1.4)$$

where the only new parameter is σ_{CI} , the collisional cross-section between free electrons and A^{+x} ions. The density squared dependence of the collisional ionization rate makes it the dominant process in high density plasmas, while the linear dependence of the photoionization rate makes it the dominant process in a low density plasma in a radiation field.

The last piece of information Equation (1.3) contains is the temperature dependence of the photoionization rate - there isn't a direct one. Since ionization is carried out by photons from some outside source, the only temperature dependence is the indirect population of the A^{+x} state from radiative recombination. The temperature dependence is on the right side of Equation (1.3) in the product $f_v \nu$ (σ_R is also dependent on ν) where ν is the velocity and f_v is the Maxwellian velocity distribution. Increasing the temperature of a Maxwellian gas makes f_v favor larger velocities, so the integral of $f_v \nu$ increases with temperature (see Figure 1.2). This also means that small temperatures can render collisional ionization negligible relative to photoionization so long as the density is low and the radiation field is strong.

Photoionized plasmas are present in high energy photon environments with low densities and temperatures. These conditions appear in range of important physical phenomena discussed in the next section.

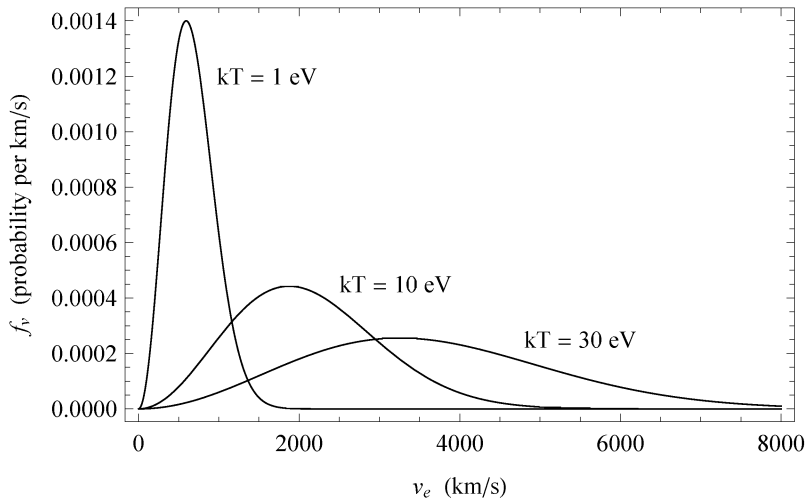


Figure 1.2: The distribution of electron velocities, f_v , for varying temperature plasmas. Temperatures are displayed as the product kT for easy comparison with ionization energy. Notice that higher temperatures correspond to faster velocities. Indeed, for a Maxwellian velocity distribution, the thermal velocity increases as the square root of temperature ($\frac{1}{2}m_e\langle v^2 \rangle = \frac{3}{2}kT$).

Table 1.1: Ionization Balance Parameters

Parameter	Definition	Units
A^{+x}	Atom of type A ionized x times	none
$n_{A^{+x}}$	Number density of A^{+x}	cm^{-3}
n_e	Number density of electrons	cm^{-3}
$h\nu^*$	Ionization energy of A^{+x}	erg
σ_{PI}	photoionization cross section	cm^2
σ_{CI}	collisional ionization cross section	cm^2
σ_R	recombination cross section	cm^2
\mathcal{N}_ν	Flux/ $h\nu$	$\text{cm}^{-2}\text{s}^{-1}$
f_v	Maxwellian velocity distribution $= \frac{4}{\sqrt{\pi}} \left(\frac{m_e}{2kT}\right)^{3/2} v^2 e^{-m_e v^2/2kT}$	s cm^{-1}
v	electron velocity	cms^{-1}

1.2 The Importance of Photoionized Plasmas

Several important astrophysical systems that contain photoionized plasmas are X-ray binaries, gas near accretion powered objects, and the HII regions surrounding luminous stars. The ten year old orbiting X-ray telescopes, the Chandra X-ray Observatory ($0.5''$ resolution) and XMM Newton ($6''$ resolution, but larger effective area) have allowed astrophysicists to explore these systems in unprecedented detail.

1.2.1 High Mass X-ray Binaries

The gas surrounding a High Mass X-ray Binary (HMXB), conceptualized in Figure 1.3, is a classic example of a photoionized plasma. This binary system consists of a compact object (a neutron star or stellar black hole) accreting mass from its large companion (an O or B star - the most luminous types of star). The compact object accretes mass in two ways: stellar wind from the companion falling on to the compact object, and Roche Lobe overflow. In HMXBs, there is a figure-8 shaped region bounded by an equipotential curve called Roche Lobe that surrounds both bodies. The crossing point on the equipotential curve between the two bodies is a Lagrangian point. Roche Lobe overflow occurs when plasma from the photosphere of the companion star passes over the Lagrangian point into the region within the Roche Lobe where the compact object's gravity pulls the material in. Figure 1.3 shows an artist's conception of this process. As this plasma falls down the potential well of the compact object, gravitational energy is converted into X-rays.

The black hole in the prototypical HMXB, Vela X-1, accretes at a rate of 7×10^{-11} Solar masses per year [7]. Its X-ray luminosity is an incredible $L_x \approx 10^{36}$ erg s⁻¹ (260 times the bolometric luminosity of the sun). This accretion process is extremely efficient at producing X-rays; 25% of the rest mass energy of the accreted material is converted into X-ray energy. The only process more efficient at producing energy is matter-antimatter annihilation (100% efficiency).

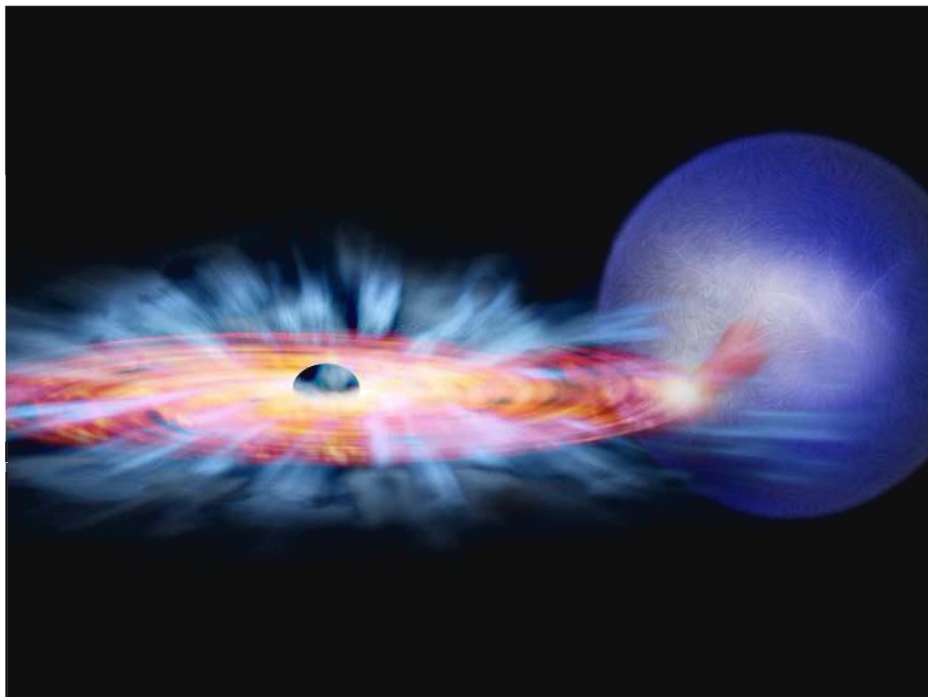


Figure 1.3: An artist's conception of a High Mass X-ray Binary (HMXB). The trail of plasma that accretes on to the compact object is the result of Roche Lobe overflow. (Image credit: NASA/CXC/M.Weiss)

The X-rays from the accretion process photoionize the material surrounding compact object,

whether it be the stellar wind from the companion or the accreting matter itself. Analyzing the photoionized material surrounding the compact object can yield a stellar mass-loss rate, the ionization balance, temperatures, ion densities and other important quantities.

1.2.2 Seyfert Galaxies

Another classic astrophysical situation where photoionization plays a dominant role is the cone of photoionized plasma perpendicular to the plane of a Seyfert galaxy (see Figure 1.4).

A Seyfert galaxy has broad emission or absorption lines from highly ionized plasmas. Seyfert 1 galaxies have both absorption and emission lines, while Seyfert 2 galaxies have only emission lines. Seyfert galaxies are thought to be irradiated by central Active Galactic Nuclei (AGN), supermassive black holes accreting material on a much larger scale than the stellar black holes in the previous example. In 1985, evidence that Seyfert 1 and 2 galaxies were in fact the same type of galaxies viewed from different orientations (Seyfert Unification Theory, see Figure 1.4) was offered [8].

X-ray observations of low temperature photoionized plasma in the Seyfert 2 galaxy NGC 1068 by Chandra (Brinkman et al. [9]) and XMM (Kinkhabwala et al. [10]) helped solidify Seyfert Unification Theory. [10] also used a unified Seyfert galaxy model to infer properties of NGC 1068 normally only observable in Seyfert 1 galaxies. Both the Chandra and XMM spectra showed the emitting plasma is relatively cold at ~ 3 eV, not enough for collisional ionization to produce the observed spectrum since transitions from ions like Ne X were observed.

[10] was able to reproduce their XMM-Newton spectra using a simple Seyfert galaxy model whose geometry is as depicted in Figure 1.4. In the model, a nuclear X-ray source (light blue sphere, obscured in center) would be shrouded by the galactic disc, but its X-rays still photoionize the cones of plasma perpendicular to the galactic plane. This photoionized plasma would then emit its own X-rays through recombination, so the Seyfert 2 observer sees emission lines in the X-ray. Because the amount of observed X-ray radiation observed from the Seyfert 2 view is directly related to the amount of material in the cone, they were able to predict the radial column density of the cone for abundant elements with transitions in the X-ray (C, N, O, Ne, Mg, and Si). Typical column densities were around 10^{18} cm^{-2} agreeing to within a factor of a few with actual observations of Seyfert 1 galaxies [11], further justifying their model.

In addition to deriving radial column densities from their photoionized cone model, [10] used the same physical model to calculate theoretical emission line profiles for plasmas under different ionization mechanisms. Figure 1.5 (originally Figure 5. in [10]) shows a theoretical series of lines from O VII (helium-like). Pure photoionization (top) produces strong resonant transitions and a Radiative Recombination Continuum (RRC). The RRC occurs because of free electrons recombining to the ground state; only cool plasmas have such narrow RRCs (recall the Maxwellians in Figure 1.2, hotter plasmas would have a larger standard deviation in energy). When only photoexcitation is included (no ionizing photons are present in the model) in the middle pane on the left, the higher n transitions like β and γ are more pronounced, since their upper levels (the $1snp$ He-like levels with dipole allowed transitions to the ground state) are populated by photoexcitation. Collisional ionization (CIE, middle left) produces a very strong $1s2p \rightarrow 1s^2$ transition, and little else.

[10] achieved an excellent fit to the XMM data using only photoionization and photoexcitation in their model, showing that collisional ionization is not an important process in the irradiated cone plasma of NGC 1068. Indeed, the widths of the RRCs constrain the temperature of the plasma to be within 2-4 eV, well below a temperature at which collisional ionization would be present.

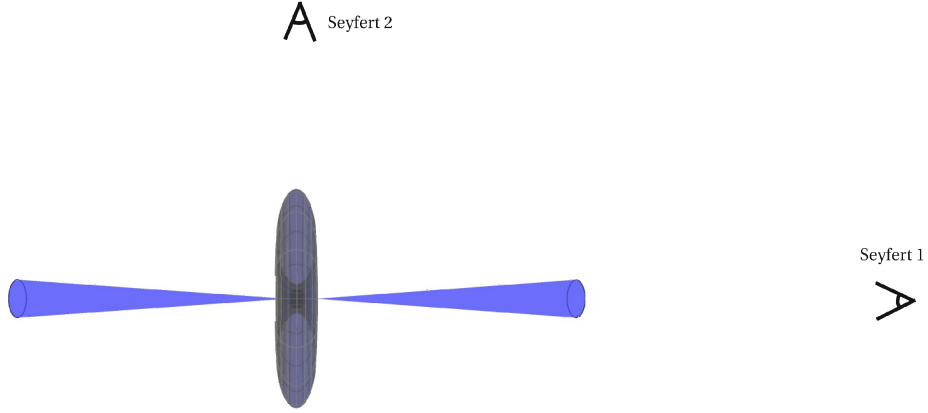


Figure 1.4: Seyfert Unification Theory. Seyfert 1 and 2 galaxies are the same object viewed from different angles. The AGN is obscured by the disc of the galaxy in this view. Observations of a Seyfert 2 galaxy show nuclear emission reprocessed by the cones (light blue). A Seyfert 1 galaxy exhibits a nuclear continuum absorbed by the cone.

1.3 Experimental Verification

The Kinkhabwala model and the models used to investigate HMXB's produce answers to important questions. However, codes like XSTAR and Cloudy that are used in many photoionization simulations have not been experimentally tested like the commonly used collisional ionization codes (APEC, for example). Indeed, these codes do not always produce identical results. Most importantly, these codes do not always produce results that match observations well [12].

Such disparities do not occur as often with collisionally ionized plasma codes because more work has gone into their verification [13]. The relative ease in producing a collisional plasma in the laboratory is a chief contributor to this disparity.

The difficulty in producing an astrophysically relevant photoionized plasma arises when attempting to produce low enough densities and a high enough X-ray flux. To see this more clearly, consider the ionization parameter²

$$\xi = \frac{4\pi F}{n_e} \quad (\text{cm s}^{-1}) \quad (1.5)$$

where F is the flux in $\text{erg cm}^{-2}\text{s}^{-1}$. Note that modulo a ratio of cross sections, ξ is essentially the volumetric photoionization rate divided by the volumetric collisional ionization rate (Divide the left side of Equation (1.3) by the left side of Equation (1.4). Once $F/h\nu$ is substituted for \mathcal{N}_ν and the integrals are dealt with, an expression similar to Equation (1.5) results) High values of ξ , therefore, correspond to situations where photoionization is likely to dominate collisional ionization.

[10] found a range of ionization parameters $\xi = 1 - 1000$ were needed to explain the spectrum they observed. The difficulty in producing a photoionized plasma with astrophysically relevant ionization parameters is compounded by the flux in the numerator of ξ and the density in the

²It is standard in astronomy to use n_i the ion density instead of n_e when defining the ionization parameter. In hydrogen dominant astrophysical plasmas they are about the same, but for the experiments described here it is more informative to use n_e .

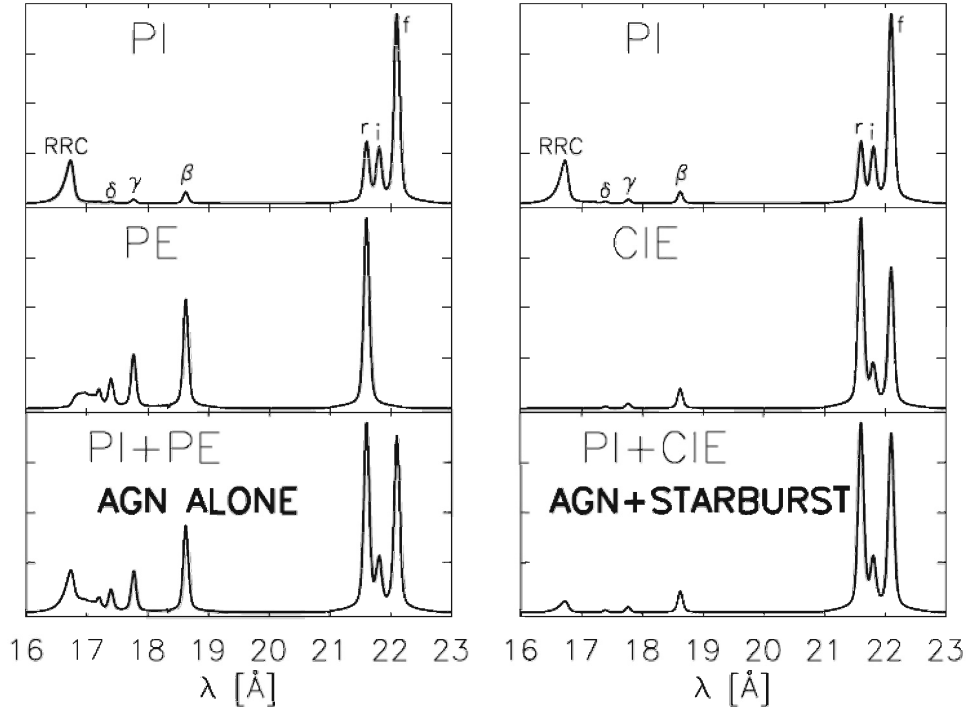


Figure 1.5: Figure 5 from [10]. PI stands for photoionization, PE for photoexcitation, and CIE for collisional ionization equilibrium. These are O VII (helium-like) lines, exhibiting a Radiative Recombination Continuum (RRC), forbidden, intercombination, and resonant lines for the $1s2p \rightarrow 1s^2$ transition and several higher order transitions to the ground state (δ for example, represents the $1s4p \rightarrow 1s^2$ transition). The PI and PE panels assume a temperature of 4 eV, while the CIE panel uses 150 eV.

denominator. In the interstellar medium for example, the density varies from 10^{-3} to 10^3 cm^{-3} [14]. At room temperature and atmospheric pressure, the density is $2.5 \times 10^{19} \text{ cm}^{-3}$. Producing a plasma with the same ionization parameter in a vacuum-less laboratory environment as in the interstellar medium may take as much as 2.5×10^{22} times more flux.³ Keeping a sample under a hard vacuum while it is bombarded with X-rays is generally not easy, so a powerful source of terrestrial X-rays is needed to produce photoionized plasmas with relevant ionization parameters. As the next section explains, a new powerful laboratory source of X-rays is just now allowing scientists to measure plasmas with ionization parameters above unity. This permits the study of astrophysical plasmas in the laboratory.

1.4 The Z Machine

The creation of photoionized plasmas in the laboratory has been made increasingly possible with the appearance of high powered laser facilities (like the Omega Laser at the University of Rochester or the National Ignition Facility) and pulsed power facilities like the Z machine at Sandia National Laboratory. The Z machine is particularly well suited for producing photoionized plasma.

³Not all photoionized plasmas are as diffuse as the interstellar medium, but the same principle holds.

The Z machine is designed to deliver a current of 20 MA to a cylindrical array of wires that lies inside a vacuum chamber. Z has a large bank of capacitors capable of storing several MJ of energy. This energy is released in approximately 100 ns, transforming the array of wires into plasma through ohmic heating.

An example array of wires is shown in Figure 1.6. The wires are made of tungsten and arranged in a cylindrical array 4 cm in diameter [15]. These wires are carefully installed in the center of the vacuum chamber at the Z machine.

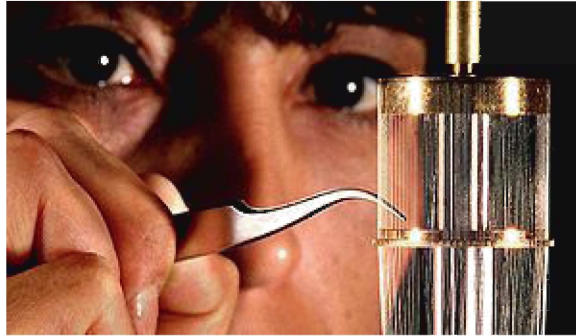


Figure 1.6: Tungsten wire array used in the Z machine at Sandia National Laboratory. The wire thickness and spacing has been optimized to maximize stability when the wire array implodes.

Once the 20 MA current has ionized the wire array into a cylindrical sheet of plasma, the plasma is free to move in response to a circumferential magnetic field. A circumferential magnetic field forms in response to the current running in a uniform direction down the z-axis of the wire array. Just as two wires with parallel currents attract, the Lorentz force generated by the magnetic field pulls the plasma symmetrically in to the z-axis (as seen in Figure 1.7).

It takes 120 ns (after the current is initially applied) for the plasma to reach stagnation on the z-axis at .2 cm in diameter, meaning the average speed of the tungsten is 150 km s^{-1} . Much of that kinetic energy is converted into X-ray photons. Indeed, in a 6 ns period around 105 ns, 1.2 MJ of energy is released in the X-ray only [15]. This method for producing X-rays is called a z-pinch. The X-ray energy radiates radially outward from the pinch.

1.5 Gas Cell Experiments

The X-rays from the z-pinch typically have enough energy to photoionize nearby gas and produce an astrophysical plasma. A gas cell filled with neon gas was placed at 5 cm from the z-axis in order to receive this ionizing radiation. The gas cell's internal dimensions are cubic with an edge length of 1 cm. Neon is filled at a density of 10^{18} cm^{-3} .

The gas cell and its relationship with the Z machine is shown in Figure 1.8. X-rays travel from the z-pinch through the side diagnostic viewing slots on the current return. From there, they go through the gas cell to be analyzed by a spectrometer. In this setup, the z-pinch acts as a backlighter for the neon in the gas cell; the spectrograph measures an absorption spectrum of the neon in the gas cell. Analyzing the spectrum of the neon after it is ionized by the z-pinch radiation

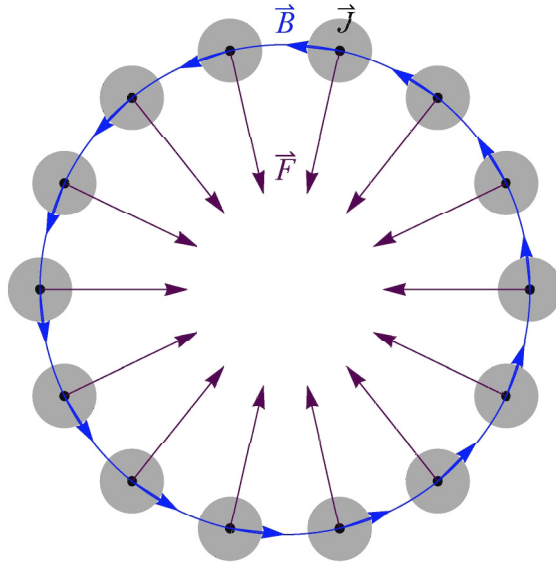


Figure 1.7: The cylindrical wire array with magnetic field (blue), current (black) and force (purple). Once the array has been ionized into a plasma, it implodes symmetrically around the z-axis. The Lorentz force felt by each volume of plasma is $\frac{1}{V}\mathbf{F} = \mathbf{J} \times \mathbf{B}$.

should accurately characterize the neon.

1.6 Statement of Purpose

The purpose of the gas cell experiments is to produce an astrophysically relevant photoionized plasma and properly characterize it. The gas experiment was designed for astrophysical relevance; neon is an abundant element that plays an important role in photoionized plasmas. As discussed in Section 1.2.2, an active galactic nucleus acts as a backlighter for the observer of a Seyfert 1 galaxy. Disregarding a difference in scale, this situation is geometrically similar to the z-pinch acting as a backlighter for the spectrograph pointed at the neon. In fact, the radial cone column densities derived by [10] are the same as the column density of neon in the gas cell, 10^{18} cm^{-2} .

The intent of subsequent chapters is to obtain the charge state distribution of the neon in the gas cell using data from the spectrograph. The motivation for this goal is simple; an accurate determination of the charge state distribution would allow for benchmarking of Cloudy, XSTAR, and other codes used by astrophysicists to model photoionization.

In Chapter 2, the physical properties of the z-pinch and the neon are examined from context of computer modeling. Rather than use forward modeling software to calculate the charge state distribution in the neon (as other have done [17, 19]), Chapter 3 introduces a model independent method for obtaining the charge state distribution of a plasma: curve of growth analysis. Chapter 4 applies this technique to the spectral data from the neon gas cell experiments.

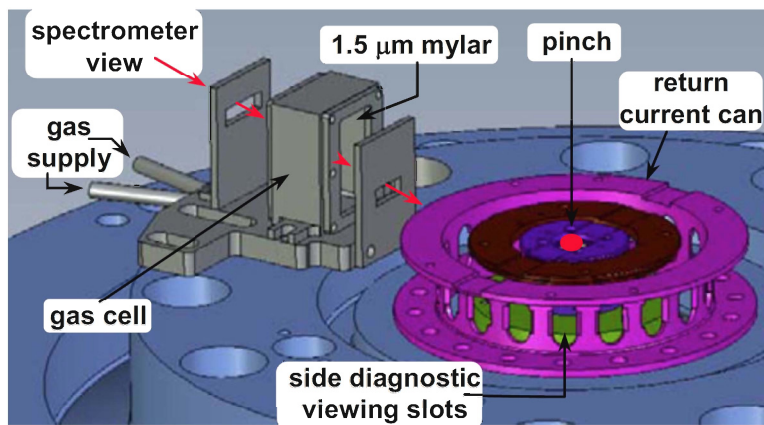


Figure 1.8: The gas cell and z-pinch. The front of the gas cell is 5 cm away from the z-axis, which runs directly through the red dot. The gas cell itself has a $1.5 \mu\text{m}$ thick mylar cover on the sides facing towards and away from the z-pinch [13]. The mylar prevents neon from escaping while still allowing most of the X-rays from the z-pinch in to the gas cell without significant reprocessing. (Image credit: Ian Hall)

Chapter 2

Computer Modeling

The physical properties of the neon are discussed in this chapter using the output from computer modeling software. Forward modeling is also considered as a means of analyzing the absorption spectrum from the neon in the gas cell, though a different model-independent method is used in the analysis presented in later chapters.

The modeling software is part of a suite of laboratory plasma modeling software written by Prism Computational Sciences. The two programs used in this chapter are VISRAD and Prism-SPECT [16]. The former allows for the simulation of the radiation environment around the imploding tungsten plasma, and the latter uses that information to simulate the conditions in the gas cell to produce a simulated absorption spectrum.

2.1 VISRAD

VISRAD takes a 3-dimensional environment and calculates the time and space dependent radiation conditions on surfaces in that environment given some specified radiation source. The user can create that environment in VISRAD using a graphical user interface.

The environment shown in Figure 2.1 was developed by Michael Rosenberg (Swarthmore 2008) for use in analyzing the gas cell experiment [17]. VISRAD deals exclusively with surfaces so each object is two dimensional. Note that the slotted current return can (gold), the apron (blue), and the floor (pink) will reprocess a substantial amount of the radiation traveling from the pinch to the gas cell. The time-dependent radius and power of the collapsing tungsten (red) for a particular z-pinch experiment¹ are used as inputs to the simulation.

Rather than solving the full radiation transport equation in all of the space in and around the experimental apparatus, VISRAD calculates the radiation properties of the surfaces only. It does this by solving a coupled set of power conservation equations for each surface. For a single surface i this equation reads

$$B_i = Q_i + \alpha_i \sum_j F_{j \rightarrow i} B_j, \quad (2.1)$$

where B_i is the radiosity of surface i , α_i is the albedo of material i , F_{ij} is the viewfactor of surface j at surface i , and Q_i is the source term for surface i [18]. The radiosity B_i is the total energy radiated per energy per time from surface i . The viewfactor $F_{j \rightarrow i}$ is the fractional amount of

¹The pinch radius and power for z-pinch shot Z-543 were measured and used as inputs here.

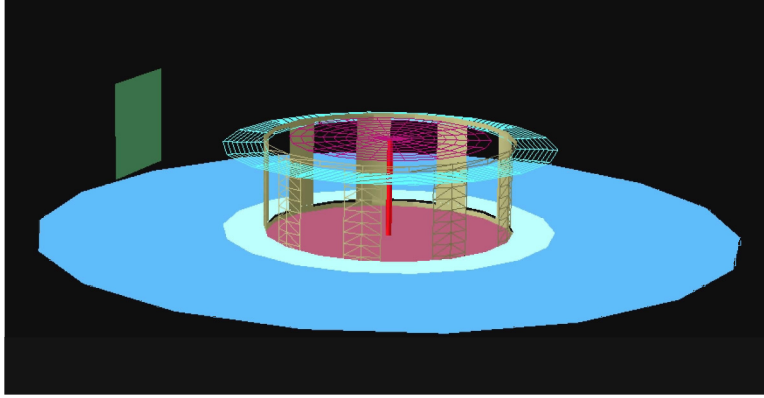


Figure 2.1: Gas cell experimental setup, designed in [17]. This setup is an idealized analog of the actual experimental setup, Figure 1.8. The tungsten plasma (red), is shown pinched here, and the front of the gas cell is represented by the green square. The partially transparent objects only appear so in this picture to reveal what lies behind. The other components are color coded as follows: apron (blue), cover (purple), floor (pink), current return can (beige), top and bottom flange (light blue).

energy leaving surface j incident on surface i . This number is purely a function of geometry, and its functional form may be found elsewhere [18]. The expression $\sum_j F_{j \rightarrow i} B_j$ is then the intensity of radiation on surface i due to the radiation from all other radiating surfaces. The source term Q_i is the intensity of radiation incident on surface i from other sources; the pinch emission is represented in this term. $F_{j \rightarrow i}$ is readily calculated and α_i and Q_i are supplied by the user, so Equation (2.1) is a matrix equation that VISRAD solves for the B_i .

Equation (2.1) is really a statement of conservation of energy. In thermal equilibrium, the net amount of energy exiting a surface i (B_i) is equal to the amount of energy reflected from other radiative sources on to surface i (Q_i) plus the amount of energy absorbed from outside sources by surface i ($\alpha_i \sum_j F_{j \rightarrow i} B_j$).

The radiation temperature (T_r) and the emission temperature (T_e) are defined as the blackbody temperatures required to produce the flux incident on a surface and the flux exiting a surface,

$$B_i = \sigma T_{e,i}^4 \quad (2.2)$$

$$\sum_j F_{j \rightarrow i} B_j = \sigma T_{r,i}^4. \quad (2.3)$$

σ is the Stefan-Boltzmann constant. VISRAD treats each surface as a radiating blackbody, so T_e in Equation (2.2) is an equivalent way of describing the blackbody radiation exiting a surface. The radiation temperature can be misleading, since each B_j is not identical and the viewfactors lower the quantity of radiation incident on a surface. For example, $\sum_j F_{j \rightarrow i}$ may have the frequency dependent distribution of several diluted hot blackbodies, but T_r describes it as a single, cooler blackbody. This means kT_r is lower than the peak photon energy $h\nu$.

Figure 2.2 shows the radiation temperature of each surface at different times during a VISRAD simulation. Significant amounts of radiation are not produced until the pinching plasma begins to

reach stagnation (Figure 2.2(d)). Much of the energy radiated by the imploding plasma is received by objects other than the gas cell. These components re-radiate at a lower temperature than the pinch, adding a softer component to the spectrum seen at the gas cell.

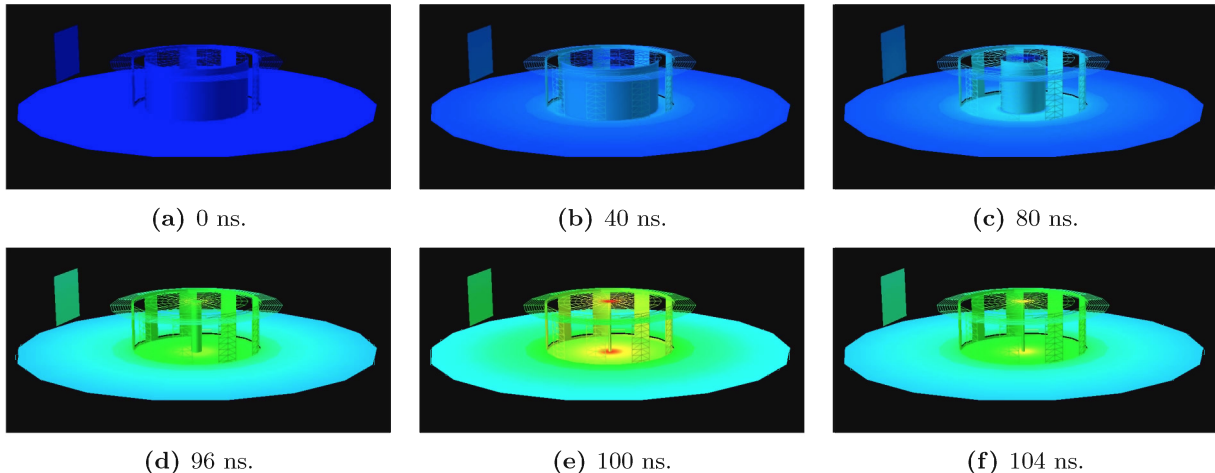


Figure 2.2: Snapshots of a VISRAD simulation at specified time-steps showing the radiation temperature, T_r . The color scale ranges from dark blue ($kT_r = 0$ eV) to bright red ($kT_r = 123$ eV). A time of 0 ns corresponds to the time at which current begins to flow through the tungsten wire array.

Those softer components are seen in Figure 2.3, where the major spectral contributions to the radiation incident on the gas cell at 100 ns are labeled. Just over half of the flux is direct radiation from the pinch - the rest is reprocessed and reduced in energy. This reprocessing is undesirable; lower energy photons can not photoionize neon into its highest ionization states (see ionization energies in Figure 1.1), a requirement for astrophysical relevance.

VISRAD can calculate the frequency dependent radiation environment at the gas cell for a specified set of time steps. The time dependent incident radiation can be used as an input to PrismSPECT, which calculates a theoretical absorption spectrum to compare with actual data.

2.2 PrismSPECT

PrismSPECT simulates the spectrum from a plasma of uniform temperature and density. It calculates the level populations in an atomic model specified by the user and synthesizes a spectrum based upon plasma conditions.

An atomic model is a list of electron configurations for each ionization stage of an element to be used in atomic calculations. The atomic model² used for the PrismSPECT investigation uses 1324 atomic configurations of neon. Every level in the VIII, IX, and X ionization stages of neon are included; detail is needed where the plasma is expected to be.

In the PrismSPECT simulation, the temperature and ion density are set to be 40 eV and 10^{18} atoms cm^{-3} respectively. The temperature, set to be the same for electron and ions, has been estimated using the 1-D hydrodynamics code Helios [19]. The ion density (number of ions of all ionization stage per cm^3) is measured by the gas cell fill pressure.

²Created using a program written by Prism Computational Sciences, the AtomicModelBuilder.

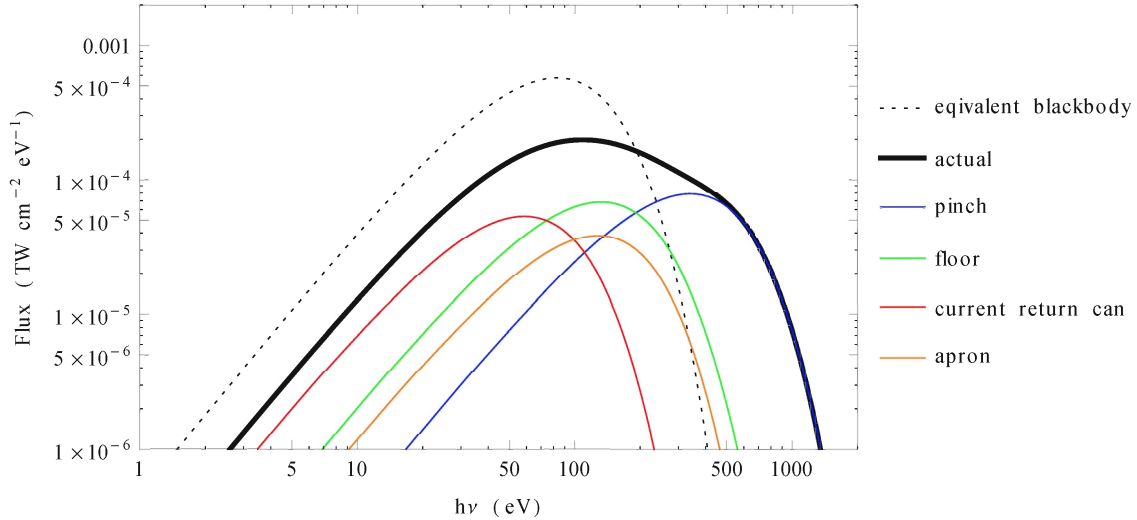


Figure 2.3: The simulated radiation incident on the center of the gas cell at 100 ns (see also Figure 2.2(e)). The thick black line shows the actual spectrum. The dotted line shows the spectrum of an equivalent blackbody ($kT_r = 29.4$ eV), a blackbody whose integrated flux is equal to the actual spectrum’s flux. The largest contributions to the actual spectrum are shown in color. 56% of the integrated flux is from the pinch. The floor (20%), current return can (10%), and apron (7%) are the next largest sources. The actual spectrum incident on the gas cell is not a blackbody itself, rather, it is a composite spectrum formed from each radiating component. The lower energy photons that cannot ionize neon are undesirable as they will heat it instead.

PrismSPECT has two level populating modes, LTE (local thermodynamic equilibrium) and non-LTE. In an LTE plasma, level populations are governed by the Boltzmann and the Saha equations. These equations are dependent only upon local parameters - temperature and density. High density plasmas with little or no incident radiation are often in LTE³. The powerful radiation from the z-pinch, however, makes it impossible for the neon in the gas cell to be in LTE. The level populating equation becomes a balance between all processes that can change the energy level of an electron - this is computationally expensive (the Boltzmann and Saha equations are comparatively cheap). If $R_{jk,Y}$ is the probability per time that a particle transitions from level j to level k due to process Y , the rate equation becomes [20]

$$\frac{dn_j}{dt} = -n_j \sum_Y \sum_k R_{jk,Y} + \sum_Y \sum_k n_k R_{kj,Y}. \quad (2.4)$$

Every excitation/ionization and de-excitation/recombination process Y must be considered. Setting Equation (2.4) to zero treats the plasma as steady-state.

PrismSPECT uses the spectrum incident on the gas cell from the VISRAD simulation to solve Equation (2.4) for each level in the atomic model. Once the levels have been populated, PrismSPECT can produce a backlit absorption spectrum. The backlighter is a 1 keV blackbody. Since the VISRAD computed spectrum is used in solving the level populations, the backlighter only functions as a medium for seeing absorption lines.

³An optically thick plasma will be in LTE. Optical depth is discussed in Chapter 3.

The resulting theoretical absorption spectrum can be seen in Figure 2.4. The most prominent line series is that of the Ne IX $1s^2 \rightarrow 1snp$ transitions, where n is the principal quantum number for the electron that transitions from the $1s$ state into the nd state after absorbing an X-ray photon. These transitions are shown schematically in Figure 2.5.

The other visible lines are produced by inner shell excitation of Ne VIII. Most of these transitions start in one of the $1s^2 2s$, $1s^2 2p$, or $1s^2 2d$ electron configurations. One of the $1s^2$ electrons is excited to an upper p or d level, an absorption transition in the X-ray.

Other simulations with higher X-ray fluxes on the gas cell have produced visible Ne X transitions; Lyman- α falls within the bandpass of the spectrograph.

The line shapes of the lines in Figure 2.4 are intrinsic to the plasma conditions, no simulated instrumental broadening has been applied. Chapter 3 will explain the broadening mechanisms in detail, but it is important to note here that the line cores for each Ne IX line is saturated (reaches essentially zero transmission) for all but the highest n lines.

Absorption lines from ions like neon are indicative of the charge state of the neon. The dominant Ne IX line series, for example, suggests much of the neon in the gas cell is Ne IX. Indeed, the PrismSPECT simulation calculates 85% of the neon is that ionization stage; the rest is Ne VIII and Ne X.

2.3 Actual Measurements

The simulated spectrum in Figure 2.4 looks a lot like the actual experimentally measured spectra in Figure 2.6. The spectra in Figure 2.6 were taken in 2001 and 2009 at the Z machine facility in Sandia National Laboratory. Each spectrum is actually the average of several sequential shots. Averaging improves the signal to noise at the cost of blending slight differences.

The actual lines aren't as narrow as those of the PrismSPECT simulation because of instrumental broadening - the spectrograph has a resolution of $800 \lambda/\Delta\lambda$. That is an uncertainty of 0.015 Å at a wavelength of 12 Å, larger than the width of most lines in Figure 2.4.

Both spectra clearly contain Ne VIII and Ne IX, and a Lyman- α line at 12.13 Å reveals the presence of Ne X. Getting the charge state from the spectrum, however, is difficult. In PrismSPECT the ion distribution was a result of solving Equation (2.4) using the simulated radiation environment at the gas cell from VISRAD. One way to get charge state information from the observed data would be to iteratively match PrismSPECT simulations to the data. The simulation that most accurately reproduces the observed spectra will give a reasonable estimate of the charge state distribution. This forward modeling approach produces satisfactory results [19], but it depends on complicated physical models and properly measured pinch conditions. The next chapter introduces a model independent procedure for obtaining the column density of an ion - an alternative way to calculate the charge state distribution.

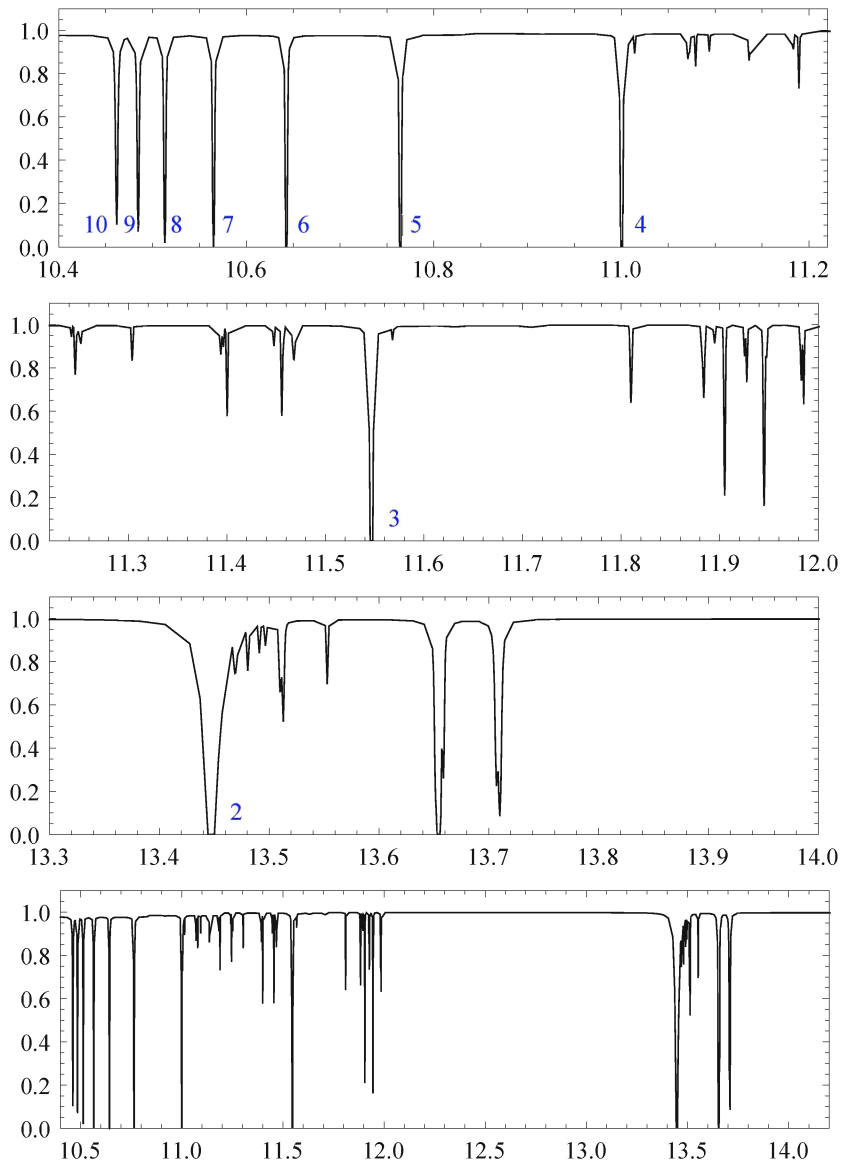


Figure 2.4: PrismSPECT simulated spectrum, transmission as a function of wavelength. The blue labels correspond to the He-like neon (Ne IX) transitions $1s^2 \rightarrow 1s nd$ where n is the number labeled in blue. In this simulation, all of the other observed lines are K-shell photoexcitations in Li-like neon (Ne VIII).

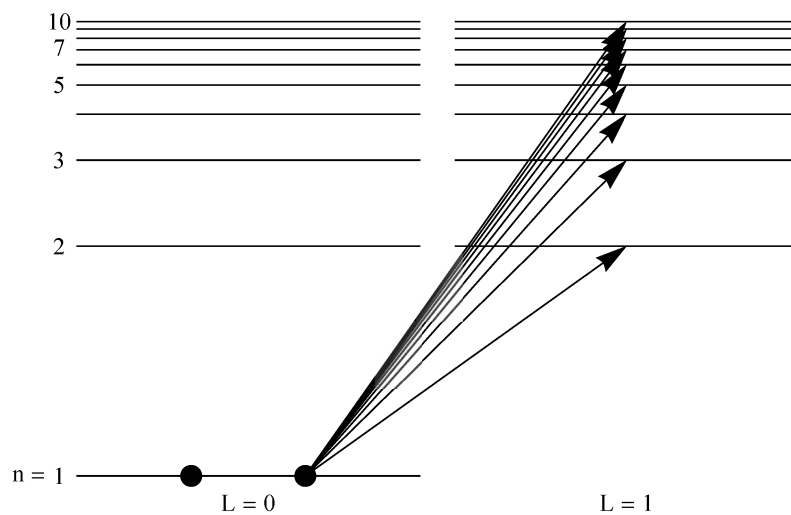
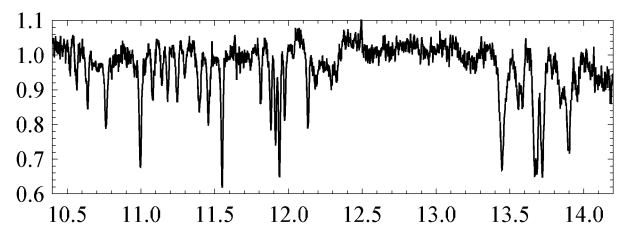
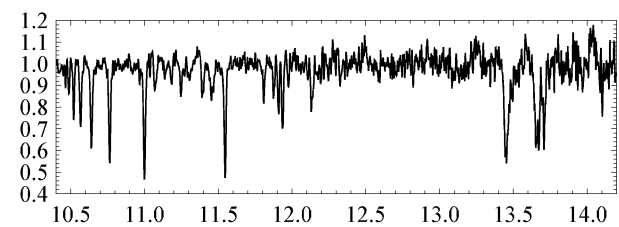
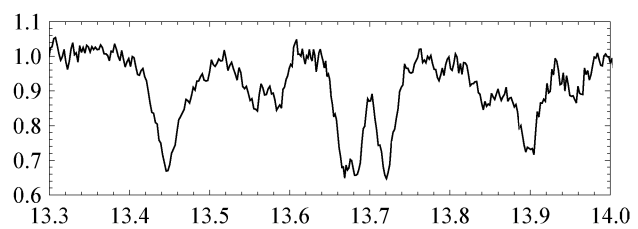
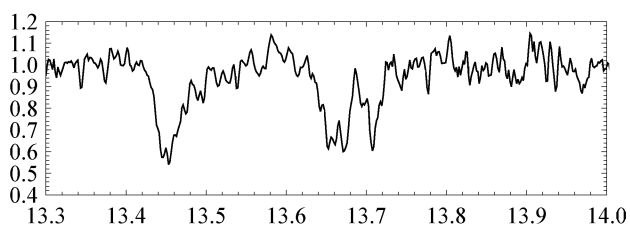
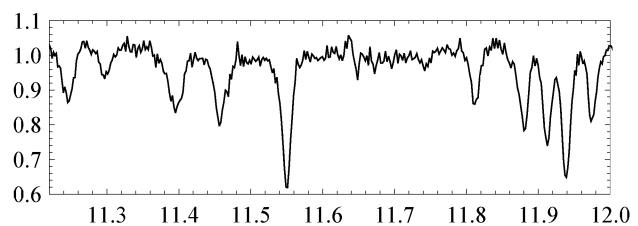
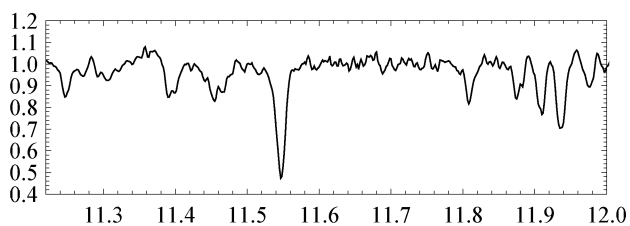
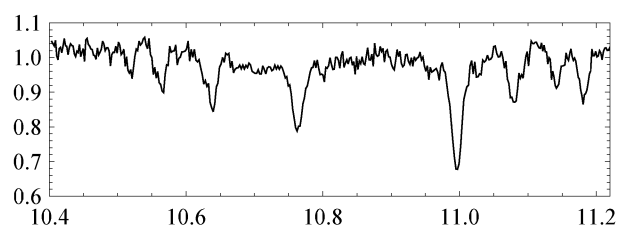
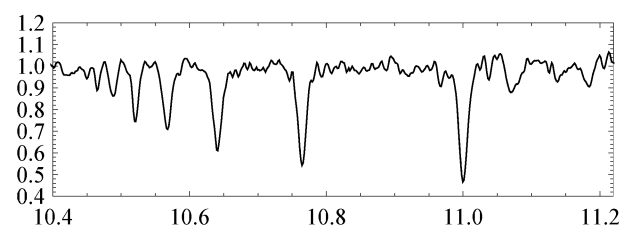


Figure 2.5: The strongest transitions for helium-like neon. The arrows indicate the change in electron energy level after the absorption of a photon.



(a) Spectrum from shots Z-541 and 543 taken in 2001.

(b) Spectrum from shots Z-1952-1954 taken in 2009.

Figure 2.6: 2001 and 2009 data without any accompanying models.

Chapter 3

Curve of Growth Analysis

As discussed in Chapter 1, the purpose of an analysis of the data presented in Figure 2.6 is to calculate the charge state distribution of the neon in the gas cell. An accurate charge state distribution could be used to benchmark codes used to analyze astrophysical photoionized plasmas. A model independent method of obtaining the charge state distribution is to use a Curve of Growth analysis to calculate the column density (and by inference the charge state distribution) of each ion in the plasma. That method of analysis is introduced in this chapter.

A Curve of Growth (COG) is a plot of W_λ/λ vs $N f_{ik}\lambda$ for all lines in a spectrum that transition to the same lower level in a particular ion. The parameters for a COG analysis are detailed in Table 3.1. To produce a COG, an observer quantifies the line strength of a series of lines by measuring their equivalent widths (W_λ) and plots them appropriately. Theoretical values for the equivalent widths of each line are fit to the measured equivalent widths with the temperature (kT) and column density (N) as fit parameters. In this manner, the column density and the temperature of an ion can be estimated. Measuring N for a series of ions from a plasma's constituent elements, like the Ne IX lines seen in the Figure 2.6 and identified in Figure 2.4, characterizes the charge state distribution of the plasma. In subsequent sections, the relationship between W_λ and N is developed to measure the column density of Ne IX in the z-pinch spectra.

Table 3.1: COG Parameters

Parameter	Definition	Units
λ	wavelength	\AA
W_λ	amount of absorption across entire line	\AA
N	ionic column density	cm^{-2}
f_{ik}	transition oscillator strength	None
kT	ionic temperature	eV

3.1 Equivalent Width

The equivalent width (W_λ) is the core concept for a COG analysis, so it will be addressed first. W_λ is a measure of the amount of absorption across an entire line-profile,

$$W_\lambda = \int_{line} \left(1 - \frac{I_\nu}{I_0}\right) d\lambda = \frac{\lambda^2}{c} \int_{line} (1 - e^{-\tau_\nu}) d\nu, \quad (3.1)$$

where I is the intensity of a line at a particular frequency and τ is the frequency dependent optical depth of the absorbing material discussed in Section 3.2. Note that the units of W_λ are \AA , but W_λ is really a measure of total absorption. The equivalent width is the width a line would be if it were a rectangle spanning from the continuum to zero transmission, as shown in Figure 3.1.

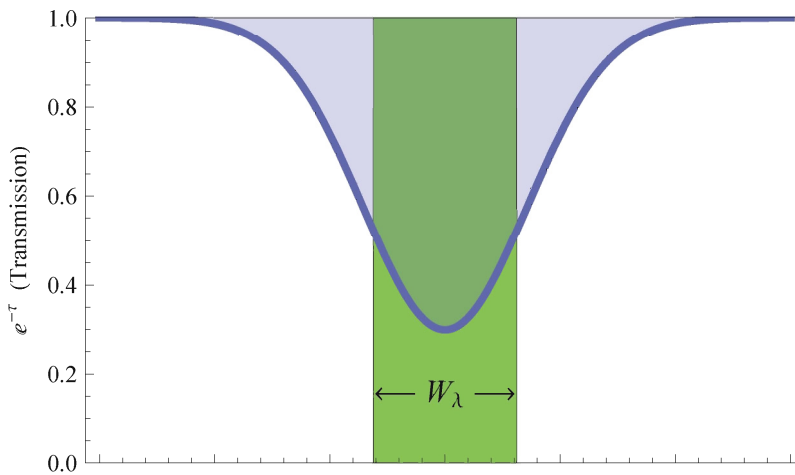


Figure 3.1: Equivalent width representation of an absorption line. W_λ is the integrated area between the line and continuum, divided by the flux of the continuum. The blue line is an example absorption line, and green region is has a widths of W_λ , so the green and blue regions have the same area.

W_λ is independent of spectral resolution, so if an instrument cannot fully resolve a line,¹ a COG can still be used to estimate N . The COG technique matches the equivalent width of a theoretical line-profile to the measured W_λ for several lines from the same lower level electron configuration. N and kT are varied for a series of model lines until the equivalent width of the model lines match the equivalent width of the actual lines. Estimates of both N and kT may be extracted from a fit, though W_λ (and therefore the COG itself) is more sensitive to N .

While W_λ is independent of spectral resolution, it is not independent of line shape. It will be shown in Section 3.3 that the variation in line shape is crucial to the fitting of a theoretical curve of growth.

¹Like the spectrometer used at the Z facility.

3.2 Optical Depth

The value of τ_ν , the optical depth at a particular frequency, dictates how absorbed the spectrum is at that frequency. An expression for τ_ν is derived using a microscopic model of absorption, in which atoms of number density n inhabit a cylinder of length ds and cross sectional area dA (Figure 3.2). The fractional amount of energy removed in a given amount of time dt from a group of photons

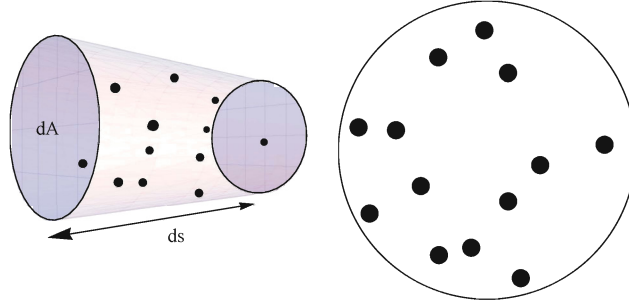


Figure 3.2: On the left is a cylinder of cross sectional area dA and length ds . There are $nds dA$ particles in the cylinder, where n is the ion density in particles cm^{-3} . On the right is the view down the cylinder, where we can see that each particle takes up σ_ν amount of area.

traveling through the volume $dA ds$ within the solid angle $d\Omega$ is equal to the number of absorbers times the cross section per absorber. There are $ndA ds$ absorbers in the volume and σ_ν represents the cross section per absorber. The energy absorbed by the particles within a frequency range $d\nu$ is then [4]

$$-dI_\nu dA d\Omega dt d\nu = I_\nu (n\sigma_\nu dA ds) d\Omega dt d\nu \quad (3.2)$$

where the negative sign arises because energy is lost. Canceling yields

$$dI_\nu = -n\sigma_\nu I_\nu ds. \quad (3.3)$$

The most general solution for I_ν must be left as

$$I_\nu(s) = I_\nu(0) e^{-\int_{s_0}^s n(s')\sigma_\nu(s') ds'} \quad (3.4)$$

where the integration has been carried along the line of sight. The integral in the exponent of Equation (3.4) is called the optical depth, τ_ν :

$$\tau_\nu(s) = \int_{s_0}^s n(s')\sigma_\nu(s') ds'. \quad (3.5)$$

This expression gives the optical depth of the material between the zero point s_0 and the point s . When σ_ν is assumed to be spatially constant, it can be brought out of the integral. In this case the previously discussed column density, N , is defined as the integral of the density,

$$\tau_\nu = N \sigma_\nu \quad (3.6)$$

$$N = \int_{s_0}^s n(s') ds'. \quad (3.7)$$

Creating a COG is as simple as using Equations (3.1) and (3.6) for a series of lines. All that remains is calculating the frequency dependence of σ_ν . In the next section, the line-profile function is introduced for this purpose.

Table 3.2: Optical Depth Parameters

Parameter	Definition	Units
τ_ν	optical depth at ν	None
n	ion density	cm^{-3}
I_ν	Intensity at ν	$\text{ergs s}^{-2}\text{cm}^{-2}\text{sr}^{-1}$
σ_ν	ionic cross section at ν	cm^2

3.3 Line-profile Functions

Absorption lines resulting from photoexcitation represent an intrinsically discretized energy change, but the theoretical profile for the optical depth is never a delta function. Instead, optical depths are proportional to a line-profile function, $\phi(\nu)$, normalized to unity

$$1 = \int_0^\infty \phi(\nu) d\nu. \quad (3.8)$$

With this definition, Equation (3.6) for the frequency dependent optical depth can be written as

$$\tau_\nu = N \sigma \phi(\nu), \quad (3.9)$$

where $\sigma = \int \sigma_\nu d\nu$. For a photoionized plasma,

$$\sigma = \frac{\pi e^2}{m_e c} f_{jk} \quad (3.10)$$

where f_{jk} is the upward² oscillator strength (from energy level j to k), a quantum mechanical correction factor to the absorption cross section of a harmonic oscillator derived from classical electrodynamics [20]. This formulation puts the frequency dependence of the intensity entirely in the line-profile function (recall the intensity is given as $I_\nu/I_0 = e^{-\tau_\nu}$). The product $N\sigma$ controls overall line strength.

Line broadening mechanisms are the physical processes that govern the shape of $\phi(\nu)$. They often fall into two general categories, those that make $\phi(\nu)$ a Lorentzian, and those that make $\phi(\nu)$ a Gaussian.

In general, mechanisms that produce both distributions are important in an absorbing plasma. Line modeling must therefore be done with a convolution of a Lorentzian and a Gaussian; the resultant distribution is called a Voigt profile. Figure 3.3 compares each of the three profiles.

The next two sections (Sections 3.3.1 and 3.3.2) derive the Gaussian and Lorentzian line-profiles from their associated broadening mechanisms. Zeeman splitting and Stark broadening are subsequently considered. Each line-profile will be derived in the context of emission, though each emission line-profile derived is equally applicable to absorptions lines.

²The directional qualification distinguishes between absorption and emission processes, though the “downward” oscillator strength f_{kj} is proportional to f_{jk} : $f_{kj} = -\frac{g_j}{g_k} f_{jk}$, where g_j is the degeneracy of state j .

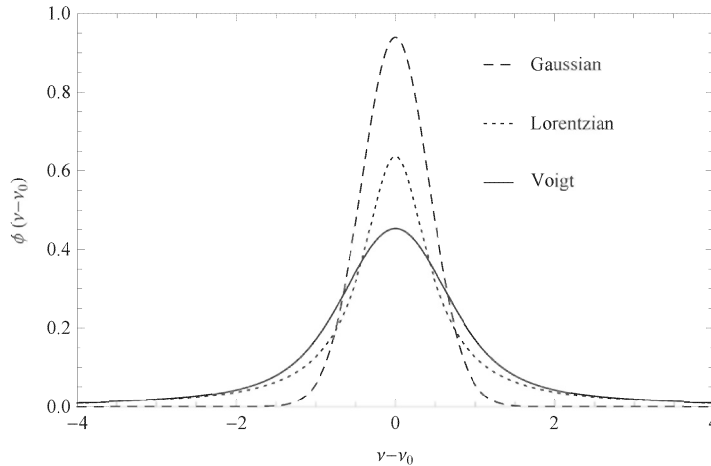


Figure 3.3: Gaussian, Lorentzian and Voigt profiles normalized to 1. Gaussian and Lorentzian curves have a FWHM of 1, while the Voigt profile is the convolution of the others. Note that the convolution of two functions is broader than the functions themselves. In a real physical model, the profile widths depend on physical parameters in a plasma. The Gaussian and Voigt profiles have a FWHM of 1 here for shape comparison only.

3.3.1 The Lorentzian Profile

In astrophysical plasmas, the most ubiquitous processes that produces a Lorentzian line-profile is natural broadening. Natural broadening can be seen as the result of the time-energy uncertainty relation and is inherent in every line; a state with a finite lifetime produces a line with a non-zero width. Collisional broadening can also produce a Lorentzian line; it occurs when an outside particle collides with an emitting atom, disrupting the phase of the emitted photon. The Lorentzian profile is derived in the context of natural broadening here.

Natural Broadening

The energy-time uncertainty relation reveals a fundamental limit on the knowledge of a state's energy, since

$$\Delta E \Delta t \gtrsim \hbar/2 \quad (3.11)$$

where ΔE is the uncertainty in a state's energy, and Δt is the lifetime of that state. All excited states have finite lifetimes, so a state's energy will never be known exactly. It follows directly that we cannot know a transition's energy exactly, so a spread of photon energies is expected.

Natural broadening is more easily discussed in the framework of classical electrodynamics than in the framework of perturbation theory, so this section will make use of the former. In the derivation that follows, an emitting atom will be modeled as an electron bound in a harmonic oscillator potential. The radiation intensity from a damped harmonically oscillating charged particle yields an emission line-profile, for the intensity of emission is proportional to the line-profile function. Thus, deriving a frequency dependent expression for the intensity $|\mathbf{E}|^2$ is the purpose of the following

derivation.

Consider the differential equation governing an electron attached to a spring of natural frequency ω_0 oscillating in space

$$-F_{rad} + \ddot{\mathbf{r}} + \omega_0^2 \mathbf{r} = 0. \quad (3.12)$$

The first term is the radiation reaction force, the force exerted on the electron by the radiation it emits.³ The radiation reaction force is given by the Abraham-Lorentz formula [21]

$$F_{rad} = \frac{\mu_0 e^2}{6\pi c} \dddot{\mathbf{r}}, \quad (3.13)$$

where it is customary to define $\tau = \frac{\mu_0 e^2}{6\pi c}$ (this constant is distinct from the optical depth, τ_ν).

Since the damping due to the radiation reaction force is small, \mathbf{r} will be approximately harmonic, $\mathbf{r} \propto \cos(\omega_0 t + \phi)$. The third time derivative of x is therefore approximated as

$$\dddot{\mathbf{r}} \approx -\omega_0^2 \dot{\mathbf{r}}, \quad (3.14)$$

giving a familiar damped harmonic oscillator differential equation

$$\ddot{\mathbf{r}} + \omega_0^2 \tau \dot{\mathbf{r}} + \omega_0^2 \mathbf{r} = 0. \quad (3.15)$$

The damped harmonic oscillator has the solution

$$\mathbf{r}(t) = \mathbf{r}_0 e^{-\gamma t/2} e^{-I\omega_0 t} \quad (3.16)$$

where the boundary condition $\mathbf{r}(0) = \mathbf{r}_0$ has been applied, and $\gamma = \omega_0^2 \tau$. An electric field with the same time component is expected,

$$\mathbf{E}(t) = \mathbf{E}_0 e^{-\gamma t/2} e^{-I\omega_0 t}. \quad (3.17)$$

As stated earlier, the intensity (proportional to $|\mathbf{E}|^2$) as a function of frequency will yield the line-profile function. A Fourier transform of \mathbf{E} in Equation (3.17) puts the electric field in frequency space,

$$\tilde{\mathbf{E}}(\omega) = \frac{1}{2\pi} \int_0^\infty \mathbf{E}(t) e^{i\omega t} dt = \frac{1}{2\pi} \frac{\mathbf{E}_0}{i(\omega - \omega_0) - \gamma/2}. \quad (3.18)$$

Squaring this field to get the intensity as a function of the angular frequency gives

$$I(\omega) = |\tilde{\mathbf{E}}|^2 \propto \frac{1}{(\omega - \omega_0)^2 + (\gamma/2)^2}.$$

Applying the normalization condition for line profile functions (Equation (3.8)) and switching from angular frequency to frequency, the Lorentzian line-profile function is proportional to the intensity,

$$I(\nu) \propto \phi_L(\nu) = \frac{\gamma/4\pi^2}{(\nu - \nu_0)^2 + (\gamma/4\pi)^2} \quad (3.19)$$

The Full Width at Half Maximum (FWHM) of the Lorentzian profile is $\gamma/2\pi$.

³All accelerating charges emit radiation, an oscillating electron is no exception.

An in depth quantum mechanical derivation of the natural broadening of a transition to a ground state shows that γ is

$$\gamma = \sum_{n'} A_{nn'}, \quad (3.20)$$

where the summand $A_{nn'}$ is the probability per unit time that spontaneous emission from the upper level n to the lower level n' will occur. $A_{nn'}$ is called an Einstein A-value. The summation is carried over all $n' < n$, so in theory a high- n state could have hundreds of terms in its sum. In practice, however, the resonance transition ($n \rightarrow 1$) usually dominates with only a few other A-values from other dipole allowed transitions contributing. Figure 3.4 shows the strongest Einstein A-values for every upper level of the Ne IX $1s^2 \rightarrow 1s np$ transitions (i.e. the $1s np$ level).

Taking the $n = 4$ (gold in Figure 3.4) level as an example, the resonant transition in the X-ray has an A-value of 10^{12} , while the next strongest transition (in the UV) has an A-value of 6.5×10^{10} , a factor of 15 smaller. This trend of decreasing A-value with increasing wavelength continues into the radio, so the sum in Equation (3.20) is dominated by only the first few terms in the X-ray and UV. For this work, the sum in Equation (3.20) was only carried over the transitions shown in Figure 3.4; low probability transitions at longer wavelengths without well documented transition probabilities in the literature were not included.

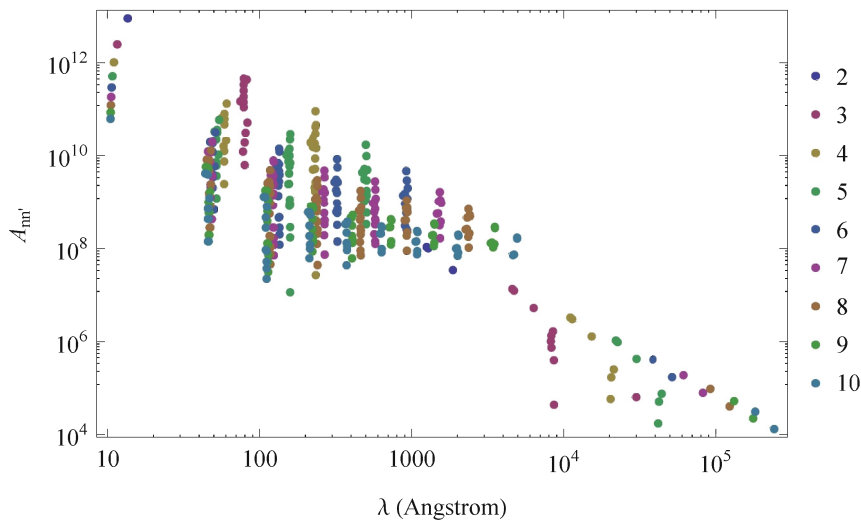


Figure 3.4: Transitions probabilities for the strongest transitions from every upper level $1s np$ in the strong Ne IX line series [1]. The colors are coded according to n , the principal quantum number of the electron in the upper level $1s np$. The X-ray transitions $1s^2 \rightarrow 1s np$ seen in the gas cell data (Figure 2.6) have the largest transitions probabilities, and only a few transitions in the UV have comparable values.

While no proof that γ is represented by Equation (3.20) is presented here,⁴ it makes sense that

⁴Hans Griem offers an excellent discussion on this and other relevant topics in his “Principles of Plasma Spectroscopy” [22].

increasing the transition probability also increases the line FWHM (note again that the FWHM is $\gamma/2\pi$). Referring back to the energy-time uncertainty relation given in Equation (3.11), $\Delta E \Delta t \gtrsim \hbar/2$, a decrease in a state's lifetime, Δt , should increase the uncertainty in its energy, ΔE (analogous to the line FWHM). Since the lifetime of a state is given as $\Delta t = 1/\sum_{n'} A_{nn'} = 1/\gamma$, an increase in γ should increase the line width, ΔE .

3.3.2 The Gaussian Profile: Doppler Broadening

The Gaussian line-profile seen in most plasmas is caused by the random thermal motion of particles in a gas. Consider a particle with some velocity v_z relative to the observer emitting a photon. The photon frequency in the particle frame, ν_0 and the frequency in the observer frame, ν , are related by the Doppler formula

$$\frac{\nu - \nu_0}{\nu_0} = \frac{v_z}{c}. \quad (3.21)$$

Since the strength of emission in a frequency range ν to $(\nu + d\nu)$ is proportional to the probability an atom has the particular v_z required to shift a line into that range, a probability distribution describing the velocities of the atoms is needed. That probability expressed as a function of frequency is the line-profile function for Doppler broadening. Maxwell-Boltzmann statistics supply the probability distribution readily [23]. The fractional number of atoms N_i in a non-degenerate gas of N atoms that have an energy E_i is

$$\frac{N_i}{N} = \frac{1}{Z} e^{-E_i/kT}, \quad (3.22)$$

where Z is the partition function for the system. The energy E_i is $E = \frac{1}{2}m(v_x^2 + v_y^2 + v_z^2)$. The number fraction in Equation (3.22) is proportional to a probability density function, $\Phi(v_x, v_y, v_z)$, which gives probability an atom has a particular velocity,

$$\Phi(v_x, v_y, v_z) = a \frac{N_i}{N} = \frac{a}{Z} e^{-m(v_x^2 + v_y^2 + v_z^2)/2kT}.$$

In the above equation, a is the constant of proportionality. Φ easily separates into three independent probability density functions, one for each velocity component,

$$\begin{aligned} \Phi &= \phi_x \phi_y \phi_z \\ \phi_i(v_i) &= \left(\frac{a}{Z}\right)^{1/3} e^{-mv_i^2/2kT}. \end{aligned}$$

A normalized version of the function ϕ_z is the probability density for an atom having a particular v_z . To recast ϕ_z as a line-profile function, it must be a normalized function of frequency. The Doppler formula (Equation (3.21)) gives the transformation to frequency from velocity,

$$\phi_z(\nu) = \left(\frac{a}{Z}\right)^{1/3} e^{-mc^2(\nu - \nu_0)^2/2\nu_0^2 kT}.$$

Applying the normalization condition, Equation (3.8), yields the Doppler broadening line-profile function

$$\phi(\nu) = \frac{1}{\delta\sqrt{\pi}} e^{-(\nu - \nu_0)^2/\delta^2}, \quad (3.23)$$

where δ is the Doppler width,

$$\delta = \frac{\nu_0}{c} \sqrt{2kT/m}. \quad (3.24)$$

In some astrophysical contexts, a macroscopic velocity field in the emitting plasma can also contribute to line broadening. The effect of this turbulence can be modeled as a Gaussian. In the laboratory, however, these turbulent effect are expected to be negligible.

3.3.3 The Voigt Profile

When Gaussian and Lorentzian mechanisms are present in a plasma, a convolution of the two distributions is the appropriate line-profile function. The result of such a convolution is termed a Voigt profile. Implicit in the assumption that the functional form of a more realistic line-profile may be calculated from the convolution of profiles arising from different physical mechanisms is the assumption that those physical mechanisms are independent. This assumptions is normally valid, except in some dense plasmas.⁵

Having dealt with the mathematical requirement for the convolution of two line-profiles, the execution of the convolution is straightforward. The convolution of two functions, f and ℓ , is

$$g * \ell(x) = \int_{-\infty}^{\infty} g(x') \ell(x - x') dx'. \quad (3.25)$$

The Gaussian and Lorentzian profiles in Equations (3.23) and (3.19) can be substituted for the functions g and ℓ in the above definition, and the resulting profile is called a Voigt profile.

$$\phi_V = \phi_G * \phi_L = \frac{\gamma}{4\pi^2 \delta \sqrt{\pi}} \int_{-\infty}^{\infty} \frac{e^{-(\nu' - \nu_0)^2 / \delta^2}}{(\nu - \nu' - \nu_0)^2 + (\gamma/4\pi)^2} d\nu'$$

Introducing the Voigt function can make this equation more compact,

$$V(x, y) = \frac{y}{\pi} \int_{-\infty}^{\infty} \frac{e^{-t^2}}{y^2 + (x - t)^2} dt. \quad (3.26)$$

The Voigt profile is proportional to the Voigt function,

$$\phi_V = \frac{V(x, y)}{\delta \sqrt{\pi}}, \quad (3.27)$$

with

$$x = \frac{\nu - \nu_0}{\delta}, \quad (3.28)$$

$$y = \frac{\gamma}{4\pi\delta}. \quad (3.29)$$

There is no closed form solution to the Voigt function, so many algorithms have been developed to approximate it [24]. An alternative approach to approximation is to realize that the Voigt function can also be represented as the real part of $w(z)$, the Faddeeva function [25]

$$w(z) = \frac{i}{\pi} \int_{-\infty}^{\infty} \frac{e^{-t^2}}{z - t} dt = e^{-z^2} \operatorname{erfc}(-iz) = V(x, y) + iL(x, y), \quad (3.30)$$

⁵In some high density plasmas collisional effects (Lorentzian profile) and Doppler shifting effects (Gaussian) interact to produce what is known as collisional narrowing [22].

where $z = x + iy$ and the complementary error function, erfc , is defined as

$$\operatorname{erfc}(z) = 1 - \frac{2}{\pi} \int_0^z e^{-t^2} dt. \quad (3.31)$$

This formalism is valid for all x and y greater than 0. While it seems that one integral representation of the Voigt profile has been substituted for a more complicated one, the new formalism is actually superior. The complementary error function is a built-in function in many mathematical modeling software packages, and can therefore be quickly and accurately calculated with no additional work required on the part of the user. This work uses the above formalism for line modeling.

To summarize, the Voigt line-profile function, ϕ_V , is calculated as

$$\phi_V(x, y) = \frac{\operatorname{Re}[e^{(x+iy)^2} \operatorname{erfc}(-x - iy)]}{\delta\sqrt{\pi}} \quad (3.32)$$

with x and y defined in Equations (3.28) and (3.29), and δ defined below Equation (3.23).

3.3.4 Zeeman Splitting

It is possible that the lines observed in the neon spectra from the z-pinch exhibit Zeeman splitting; a magnetic field could be broadening spectral lines. Since the tungsten wire array is inundated with 20 MA of current, a large magnetic field is created outside of the collapsing tungsten plasma. The slotted gold current return can surrounding the wire array is designed in part to prevent stray magnetic field from escaping into the gas cell, but inevitably some does escape.

Zeeman splitting would invalidate a Voigt profile model for the neon spectral lines, so it needs to be considered. Energy level splitting will be compared to the Doppler width δ (an underestimate of the Voigt width), defined in Equation (3.24).

The Hamiltonian for an atom in a magnetic field is given as

$$H = H_0 + H_{FS} + H_Z \quad (3.33)$$

Where H_0 is the standard energy operator, H_{FS} is the fine structure operator (a combination of the spin-orbital operator and a relativistic correction), and H_Z is the term added to account for the Zeeman effect.

The standard procedure for calculating the energy splitting due to a magnetic field is to treat both H_{FS} and H_Z perturbatively (this is the Weak Field Approximation). The energy level splitting of an electron due to a magnetic field of strength B between is [26]

$$\Delta E = gM\mu_B B \quad (3.34)$$

where g is the Landé-g factor for the electrons energy level and μ_B is the Bohr magneton. The projection of the total angular momentum in the z-direction, M , takes on any of the $2J(J+1)$ integer spaced values, $\{-J, -J+1, \dots, J\}$.

This change in energy can be estimated for typical plasma parameters. For the helium-like neon in the gas cell, the only noticeable transitions have $J = 1$ in their upper level, since the lower level

is the ground state.⁶ The Landé g-factor for these transitions is 3. Therefore, the energy spacing between the two farthest apart levels after splitting is

$$\Delta E = 2(3 \times 1 \times \mu_B B) = 3.48 \times 10^{-10} B \text{ eV/Gauss.} \quad (3.35)$$

At a wavelength of 12 Å, this is a wavelength difference of

$$\Delta \lambda = \frac{\Delta E \lambda^2}{hc} = 4 \times 10^{-10} \text{ Å/Gauss.} \quad (3.36)$$

The FWHM of a Doppler broadened spectral line from a 30 eV neon plasma is much larger than that:

$$\Delta \lambda_{1/2} = \lambda_0 \sqrt{\frac{8 \ln(2) kT}{m c^2}} = 1.1 \times 10^{-3} \text{ Å.} \quad (3.37)$$

This means a magnetic field of $B \approx 3 \times 10^6$ Gauss in the gas cell would be needed to produce Zeeman splitting comparable to the Doppler width. This field strength is impracticably large. In fact, it is larger than the unabated field 5 cm away from a wire with 20 MA of current, the extreme upper bound for the field strength in question,

$$B_{max} = \frac{\mu_0 I}{2\pi r} = 8 \times 10^5 \text{ Gauss.} \quad (3.38)$$

Zeeman splitting does not need to be included in spectral analysis.

3.3.5 Stark Broadening

An additional broadening mechanism could be present in the photoionized neon spectra from the gas cell, Stark broadening.

On a large scale, plasmas are usually neutral and produce no net electric field. However, on a small scale, electrons and ions create a dynamic electric *microfield*. This microfield can split the atomic energy levels in an ion (the Stark effect) and consequentially the energy of an absorbed or emitted photon, affecting a spectral line in what is known as Stark broadening. The specific value of the microfield changes rapidly and would be difficult to calculate for each emitting ion in a plasma, so spectroscopists have attempted to approximate the probability distribution for the electric microfield [27]. This probability distribution is required to model the line profile of a Stark broadened line.

In order to approximate the line-profile of a Stark broadened line, each emitting ion is taken to be static [22]. In this approximation the line shape is given as [28]

$$\phi_{Stark}(\nu) = \int_0^\infty P(\varepsilon) J(\nu, \varepsilon) d\varepsilon \quad (3.39)$$

where $P(\varepsilon)$ is the probability of finding the electric microfield as the magnitude ε and $J(\nu, \varepsilon)$ is the line-profile for an emitting ion in the presence of the field ε . A detailed approximation of $P(\varepsilon)$ or $J(\nu, \varepsilon)$ is beyond the scope of this document, though an approximation to $J(\nu, \varepsilon)$ can be calculated using standard perturbation theory and yields a closed form expression [29].

⁶Dipole allowed transitions must have $\Delta J = 1$ and the ground state has $J = 0$, so the most powerful transitions all originate in $J = 1$ upper levels.

The difficulty in calculating the Stark broadened line-profile lies in approximating $P(\varepsilon)$. As discussed above, the electric microfield is due to both ions and electrons. The ions (low thermal speed) supply a low frequency field, while the electrons (high thermal speed) supply a high frequency field. Both components and their interaction must be accounted for if $P(\varepsilon)$ is to be properly estimated. In the late 1980s, a successful theory was developed to estimate $P(\varepsilon)$ and an accompanying code (the Adjustable Parameter Exponential code - APEX) was created for its evaluation [27]. An example output of the code for a two species plasma is shown in Figure 3.5. The specifics of the probability distribution are unimportant, but the agreement between the theoretical code and Monte Carlo simulations is significant. The advantage of the APEX code is portability and speed as compared with a simulation: it is easier to integrate the APEX code into a spectral analysis.

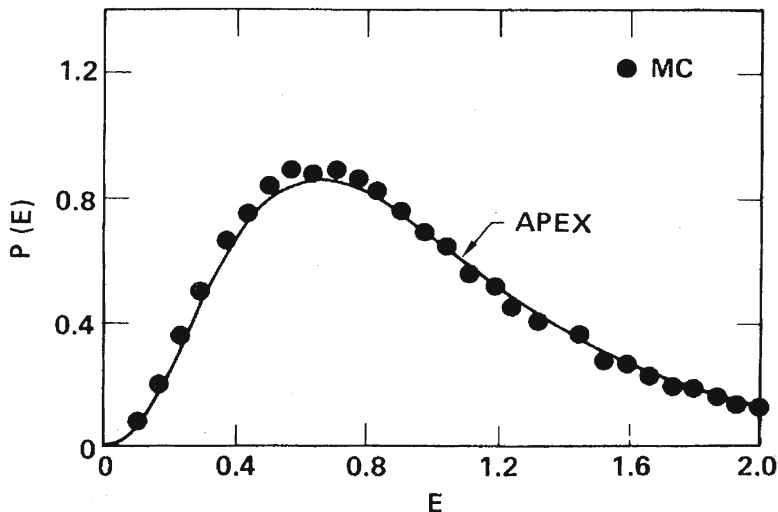


Figure 3.5: The probability distribution for the electric field, ε , calculated using the Adjustable Parameter Exponential code (APEX). Figure from [27]. The field at an ion of charge $Z = 17$ was calculated in a two species plasma ($Z = 1, 17$). ε is in units of $\varepsilon_0 = e \left(\frac{4\pi n_e}{3} \right)^{2/3}$, where n_e is the free electron density and e is the elementary charge. The theoretical APEX model agrees well with the Monte Carlo simulations (black circles).

An example of the line-profile function produced by Equation (3.39) are shown in Figure 3.6. When only the low frequency (due to ions) field is included in the theory as in (a), the line-profile exhibits bimodal behavior indicative of the Stark effect. Including the high frequency broadening in (b) adds a peaked line center. Adding Doppler broadening increases the line width in (c).

Stark broadening can be included in a spectral analysis by convolution. For example, to include Stark broadening and a Voigt profile, the line profile function would be

$$\phi(\nu) = \int_{-\infty}^{\infty} \phi_{Stark}(\nu') \phi_{Voigt}(\nu - \nu') d\nu'. \quad (3.40)$$

Since the distribution $P(\varepsilon)$ from the APEX code is a numerical result, this convolution would not have an analytic solution like the Voigt profile in Equation (3.32). Instead, it would be a numerical convolution that would be evaluated each time a new line is modeled.

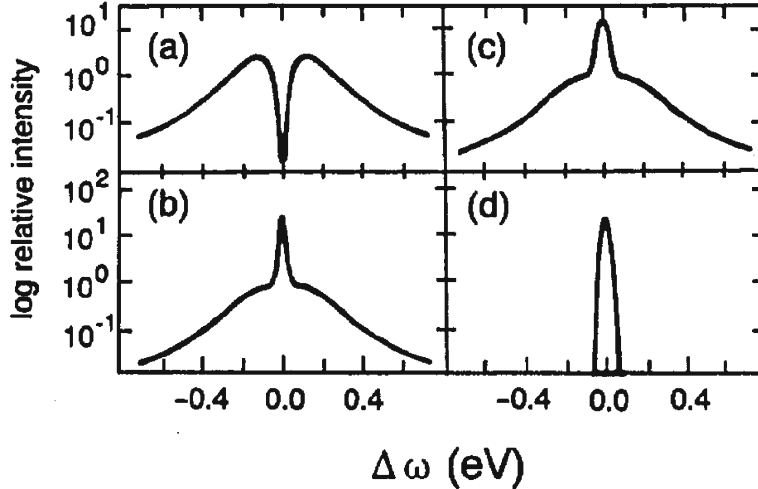


Figure 3.6: Stark broadening line-profile functions for Ne X Ly- α . Figure from [28]. (a) Profile with only ion (low frequency) microfield. (b) Ion and electron microfields included. (c) Same as (b) convolved with a Gaussian. (d) A Gaussian by itself.

Stark broadening is not a factor in most astrophysical plasmas; the density is too low to create significant microfields. This is especially true in astrophysical photoionized plasmas, where densities tend to be quite low. However, since the density of neon in the gas cell experiment ($n = 10^{18} \text{ cm}^{-3}$) needs to be much higher than an astrophysical plasma to obtain a measurable absorption signal in a 1 cm thick gas cell, Stark broadening is expected to be significant [30].

The effect of Stark broadening on the neon lines in the gas cell absorption spectra is actively being investigated. A preliminary analysis of Stark broadening is presented in Chapter 4.

3.4 An Example Curve of Growth

Using the theory of line broadening discussed above, a COG analysis is performed on an idealized set of data in this section. In a classic COG, a Voigt profile is assumed valid for each absorption line.

A COG analysis is most powerful when a series of absorption lines from the same lower energy level are available. Take, for example, the lines over plotted in Figure 3.7. Each line uses exactly the same Voigt line-profile,⁷ only the absorption cross section σ increases to saturate the lines. This pattern is often seen in real spectral data where a series of lines have a range of oscillator strengths (much like the transitions probabilities in Figure 3.4).

The Voigt profile produces three distinct line shapes, depending on how saturated the line is. For unsaturated lines (red), the line shape is essentially an inverted Gaussian profile. The inversion arises because the exponential representing the intensity, $e^{-N\sigma\phi_{\text{Voigt}}(\nu)}$, is approximately linear at small optical depths. An inverted Gaussian profile appears at low optical depths because

⁷In an actual spectral analysis like the one seen in the next chapter, the parameter γ varies from line to line changing the shape of the Voigt line-profile as well.

only the core of the Voigt profile is noticeable, and the core of a Voigt profile is dominated by its Gaussian constituent. The green lines indicate the saturation of the line core. The Voigt profile is still dominated by its Gaussian constituent since we see narrow line wings. The final set of lines shows saturation of the line wings. Referring back to Figure 3.3 where Gaussian, Lorentzian, and Voigt line-profiles are compared, it is clear that the line wings in the Voigt profile come from the Lorentzian profile. These wings are called Lorentzian wings.

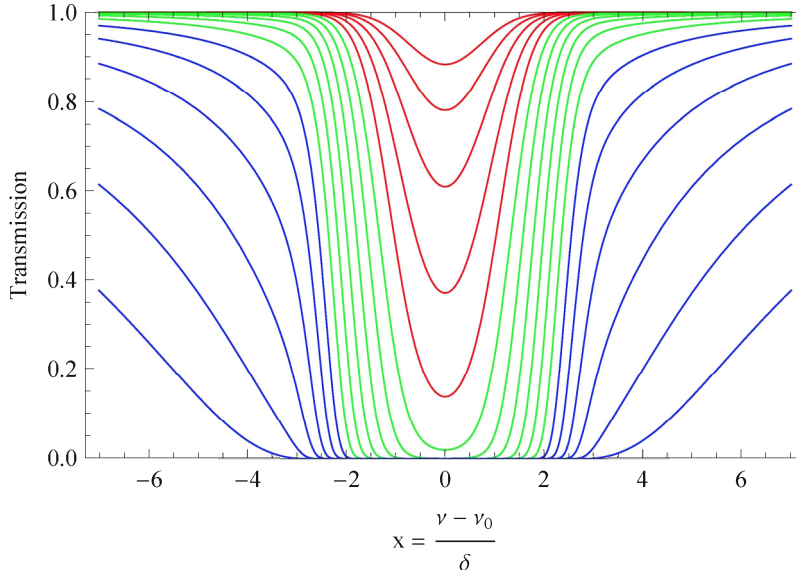


Figure 3.7: A set of idealized Voigt absorption lines over plotted (in a real spectrum the lines would hopefully be well separated). The absorption lines have the form $I/I_0 = e^{-N\sigma\phi_{\text{Voigt}}(\nu)}$, and σ is steadily increased to saturate the lines. The x-axis is in units of x , the Voigt parameter (Equation (3.28)). The red lines are unsaturated, the green lines have saturated line cores, and the blue lines have partially saturated wings.

The equivalent widths for the lines in Figure 3.7 have been tabulated using Equation (3.1) and plotted against $N\sigma$ in Figure 3.8. This plot, showing the relationship between the equivalent width and $N\sigma$, is a curve of growth. The word curve is slightly misleading, as Figure 3.8 is a plot of points, and the number of points is limited to the number of spectral lines. It is common for COGs generated by theoretical profiles to be made continuous by fitting discrete quantities like f_{jk} and pretending a continuum of spectral lines are available for measurement.

The three different line shapes displayed in Figure 3.7 correspond exactly to the three regions in the curve of growth. In the red region, the equivalent width increases linearly with increasing σ . In this region, $e^{-\tau} \approx 1 - \tau$. Using this approximation it is easy to see that the linear relationship between W_λ and σ is in fact expected, since Equation (3.1) for the equivalent width of a line reduces to

$$\frac{W_\lambda}{\lambda} = N\sigma\lambda \quad (3.41)$$

where σ is given in Equation (3.10) as $\frac{\pi e^2}{m_e c} f_{jk}$, N is column density for the ion producing the line,

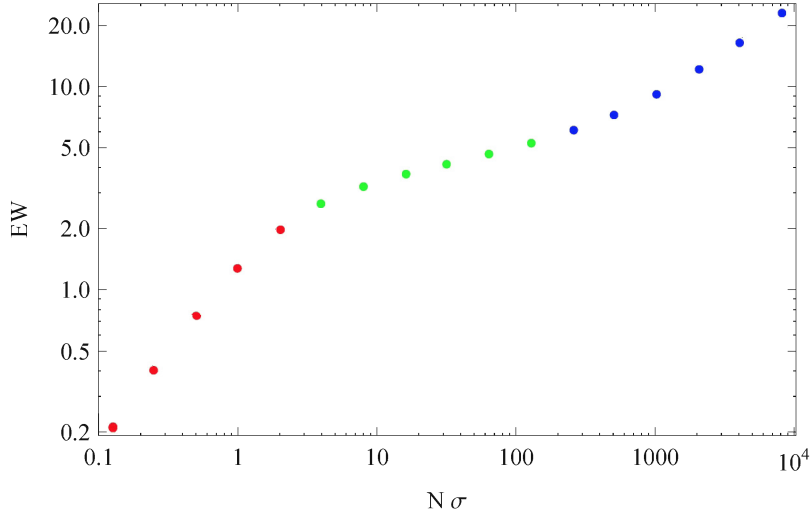


Figure 3.8: Curve of growth for the idealized lines plotted in Figure 3.7, which shares the same color coding. A COG is typically plotted on a log-log scale. The linear, log, and square root portions of the COG are red, green, and blue respectively.

and λ is the wavelength of the line. Rather than plot W_λ vs $N\sigma$, most curves of growth plot $\frac{W_\lambda}{\lambda}$ vs $Nf_{jk}\lambda$, so that the relationship has a slope of unity.

The green region is where W_λ increases the slowest, since the line core is saturated and the wings are not important yet. This region is called the “log” part of the COG, since

$$\frac{W_\lambda}{\lambda} = \frac{2b}{c} \left(\ln \left(\frac{N\sigma\lambda}{\sqrt{\pi}b} \right) \right)^{1/2} \quad (3.42)$$

where $b = \sqrt{2kT/m} = \lambda\delta$. To derive this relationship, a Gaussian line-profile must replace the more general Voigt profile [20]. As discussed above, the line is still dominated by the Gaussian broadening at this point so the approximation is reasonable.

In the blue region, the Lorentzian wings begin to dominate the equivalent width. This region is called the “square root” part of the COG, for it can be shown [20] that in this region

$$\frac{W_\lambda}{\lambda} = \frac{2}{c} \left(\lambda^2 N\sigma \frac{\gamma}{4\pi} \right)^{1/2} \quad (3.43)$$

where γ is the Lorentzian parameter defined in Equation (3.20). To derive this expression, a Lorentzian profile with parameter γ must replace the Voigt profile in the calculation of W_λ . This is a reasonable assumption since the Lorentzian wings dominate the equivalent width in the last few blue lines in Figure 3.7 (the intermediate lines are in transition, so the approximation applies for the thickest lines).

The COGs strong dependence on N is what enables accurate measurement of the column density. By measuring equivalent widths for a series of lines from an actual spectrum, an experimental plot of $\frac{W_\lambda}{\lambda}$ vs $Nf_{jk}\lambda$ can be produced. Theoretical lines (like those of Figure 3.7) to match each

experimental line could be produced and their equivalent widths calculated. The theoretical lines are dependent on N and kT , these quantities could be calculated by matching the theoretical curve of growth to the experimental one. This is the approach taken in Chapter 4.

Chapter 4

Spectral Analysis and Discussion

In order to compare a theoretical COG to one produced by plasma in the gas cell, equivalent widths of lines in an experimentally measured spectrum must be tabulated. A Voigt profile is used to compare a theoretical COG to the experimental COG in Section 4.2, along with a preliminary analysis of Stark broadening. Since the Ne IX $1s^2 \rightarrow 1snp$ line series is by far the strongest series of absorption lines, it will be used in the COG analysis for both the 2001 and 2009 data.

4.1 Equivalent Width Measurement

Calculating equivalent widths of a normalized spectrum taken with a spectrograph of infinite resolution is straight forward; the width is the area between the absorption line and the continuum intensity (recall the visualization of equivalent width in Figure 3.1). One approach to approximating this area is to fit the spectrum to I_ν in Equation (3.1),

$$\text{idealized experimental intensity} = I_0 e^{-\tau_\nu} \quad (4.1)$$

and integrate between $I_0 e^{-\tau_\nu}$ and I_0 , the continuum intensity. In Equation (4.1), the optical depth τ_ν is proportional to the Voigt line-profile function.

However, as discussed in Section 3.1, the instrumental resolution of the spectrograph pointed at the gas cell has a dominating effect on the shape of the experimental line-profile (again, this is why the curve of growth method is relevant - it is resolution independent). Thus, any theoretical line-profile function would need to be convolved with an instrumental point spread function (PSF) before Equation (4.1) is relevant.¹

The functional form of Equation (4.1) is still useful in calculating equivalent widths, as it is bounded by zero and the continuum intensity. It is therefore used to represent an absorption line in the spectrum, though a Gaussian is used in place of a theoretical τ_ν .

Ideally, post-measurement processing would flatten the background intensity to unity, but in practice there are slight deviations. These deviations tend to be locally linear, so a linear model is added to the exponential line absorption model to correct for imperfect normalization. The resulting equivalent width measurement function has the form

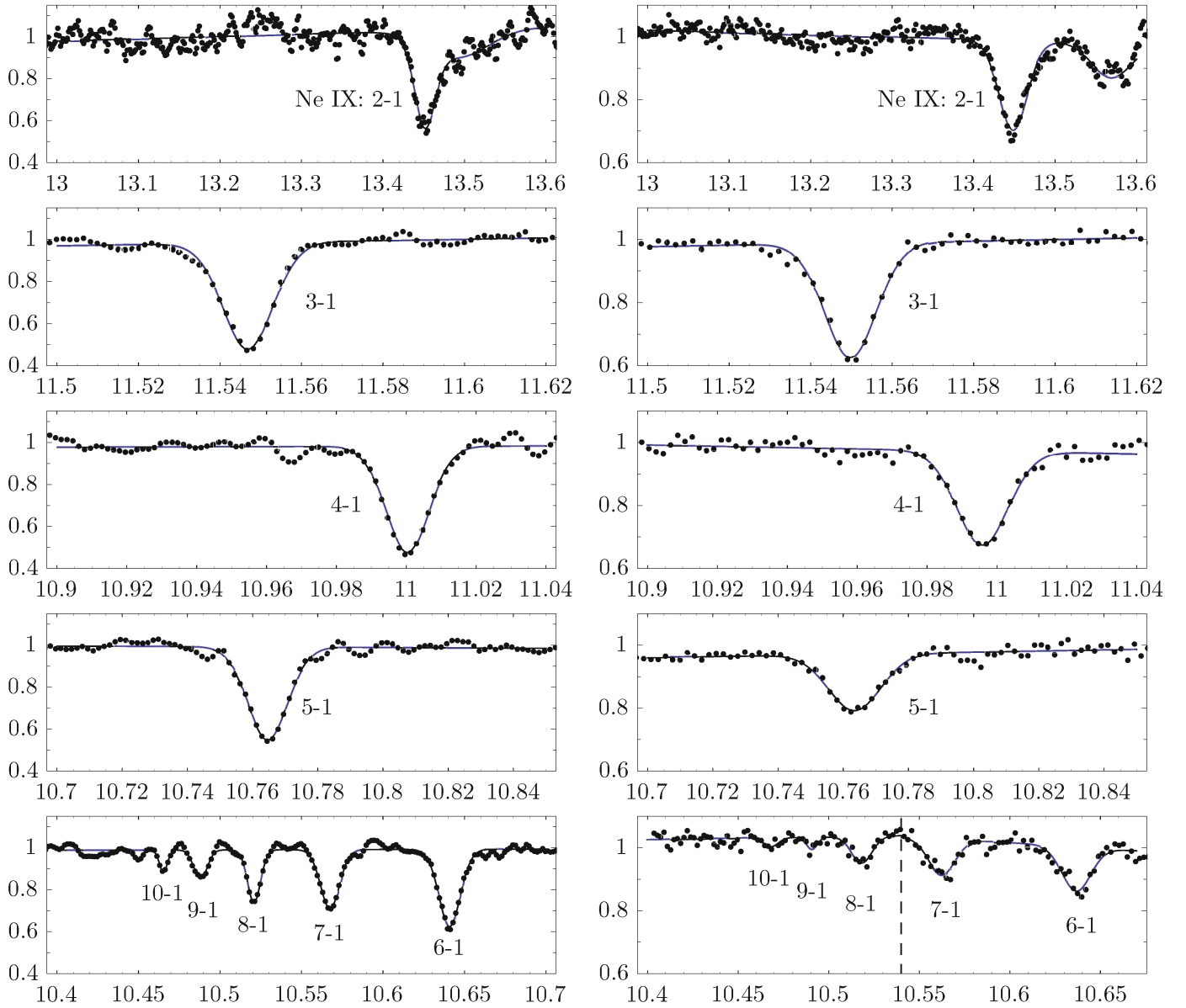
$$\text{idealized experimental profile} = m\nu + b + e^{Ae^{-\frac{(\nu-\nu_0)^2}{2\sigma^2}}}, \quad (4.2)$$

¹Currently an instrumental PSF does not exist, so an alternative approach is used here.

where a Gaussian profile with amplitude A , center ν_0 and standard deviation σ has been substituted for τ_ν . The line $m\nu + b$ is the difference between the background profile and unity.

There are three reasons a Gaussian has been chosen over any other function. First a Gaussian is simple to construct and computationally cheap to model with. A Gaussian is also the distribution the Central Limit Theorem mandates a composite probability distribution approaches. In other words, the more line-profile functions that are convolved together (Gaussian, Lorentzian, all aspects of the instrumental PSF), the more the resultant profile looks Gaussian. The last, and by far most important reason: it produces good fits to the data.

Fits to data from 2001 and 2009 are shown in Figure 4.1. The middle three rows are fit exactly with Equation (4.2). The first and last rows are fit to Equation (4.2) with additional exponential factors added for each line. In all cases, the region shown is the range over which the fit was performed on. Fits were not performed on large regions because the background fluctuations are only locally linear. The vertical line in the last row of the 2009 data separates two different models. In both the 2001 and 2009 data, two Gaussians have been used to model the Ne IX line. This is justified in the PrismSPECT simulation shown in Figure 2.4, where it is seen that additional transitions lie in this region.



(a) 2001 data: Spectra taken from shots Z-541 and Z-543 were averaged together to produce the data above. Note that the y-axes on this column of plots and the adjacent 2009 column are different.

(b) 2009 data: Averaged spectra from shots Z-1952, Z-1953, and Z-1954. The dashed line in the bottom plot indicates the division of two separate models; the left models the 10, 9 and 8 transitions, the right models the 6 and 7 transitions.

Figure 4.1: Transmission vs wavelength in Å for spectra from 2001 and 2009 fit to Equation (4.2)

The absorption lines in Figure 4.1 do not reach zero transmission, but it is incorrect to conclude that the intrinsic line profiles are not saturated. As in the PrismSPECT simulation shown in Figure 2.4, the pre-instrumentally broadened lines are mostly saturated. The instrumental broadening desaturates the lines while conserving equivalent width. Indeed, if all of the pre-instrumentally broadened lines were not saturated, the COG analysis presented in Section 4.2 would present a curve only in linear regime, similar to the red portion of Figure 3.8. Section 4.2 shows that at least

the linear and log portions of the COG seen in Figure 3.8 are seen in the data, implying that a range of saturation is present in the intrinsic line profiles.

Tables 4.1 and 4.2 contain useful fit information for data from 2001 and 2009, including the equivalent width measurements in mÅ. To calculate errors on fit parameters, individual points in the experimental spectra also need errors. Since the post measurement procedure doesn't assign errors to individual points, errors were assigned in the following manner. Two spectral regions known to have no noticeable transitions were chosen from a given spectrum. Separate linear models were fit to the points in these two spectral regions, and a standard deviation of the fit residuals was calculated in each of the two regions. The average of these two standard deviations was assigned as the error for all points in the given spectrum. This procedure is not ideal, so all errors reported in Tables 4.1 and 4.2 should be considered cautiously. It should also be noted that this procedure does not account for any systematic error associated with the type of model used to fit a line. While most lines in the spectrum obey a Equation (4.2) well, the 2-1 transition in the 2009 data for instance, does not.

Equivalent widths were calculated by using the best fit parameters for the Gaussian representing the line. To calculate the upper and lower error on the equivalent widths, upper and lower 1- σ bounds for the Gaussian's amplitude and standard deviation were used to calculate new equivalent widths. The best fit equivalent widths were subtracted from the new equivalent widths, and the difference is the error.

Table 4.1: 2001 line fit statistics

n Transition	Equivalent width (mÅ)	Measured line center (Å)	Theoretical line center (Å)
2-1	12.29 ^{+1.48} _{-1.43}	13.4513 ^{+0.0005} _{-0.0007}	13.44731
3-1	7.96 ^{+0.38} _{-0.38}	11.5467 ^{+0.0002} _{-0.0001}	11.54681
4-1	8.22 ^{+0.29} _{-0.28}	11.0003 ^{+0.0001} _{-0.0001}	11.00049
5-1	6.93 ^{+0.25} _{-0.24}	10.7646 ^{+0.0001} _{-0.0001}	10.76440
6-1	6.18 ^{+0.24} _{-0.23}	10.6410 ^{+0.0001} _{-0.0001}	10.64027
7-1	4.18 ^{+0.20} _{-0.19}	10.5675 ^{+0.0001} _{-0.0002}	10.56676
8-1	2.56 ^{+0.15} _{-0.14}	10.5209 ^{+0.0001} _{-0.0001}	10.51957
9-1	1.42 ^{+0.14} _{-0.13}	10.4881 ^{+0.0004} _{-0.0001}	10.48746
10-1	0.66 ^{+0.11} _{-0.10}	10.4653 ^{+0.0003} _{-0.0002}	10.46460

Table 4.2: 2009 line fit statistics

Transition Transition	Equivalent width (mÅ)	Measured line center (Å)	Theoretical line center (Å)
2-1	$12.75^{+0.60}_{-0.57}$	$13.4485^{+0.0004}_{-0.0004}$	13.44731
3-1	$5.83^{+0.30}_{-0.30}$	$11.5498^{+0.0002}_{-0.0001}$	11.54681
4-1	$5.67^{+0.35}_{-0.33}$	$10.9959^{+0.0002}_{-0.0002}$	11.00049
5-1	$3.74^{+0.35}_{-0.32}$	$10.7635^{+0.0004}_{-0.0004}$	10.76440
6-1	$2.77^{+0.39}_{-0.36}$	$10.6368^{+0.0006}_{-0.0005}$	10.64027
7-1	$2.06^{+0.35}_{-0.33}$	$10.5626^{+0.0007}_{-0.0005}$	10.56676
8-1	$1.28^{+0.37}_{-0.29}$	$10.5182^{+0.0007}_{-0.0006}$	10.51957
9-1	$0.34^{+0.34}_{-0.16}$	$10.4908^{+0.0001}_{-0.0001}$	10.48746
10-1	$0.29^{+0.21}_{-0.14}$	$10.4683^{+0.0002}_{-0.0002}$	10.46460

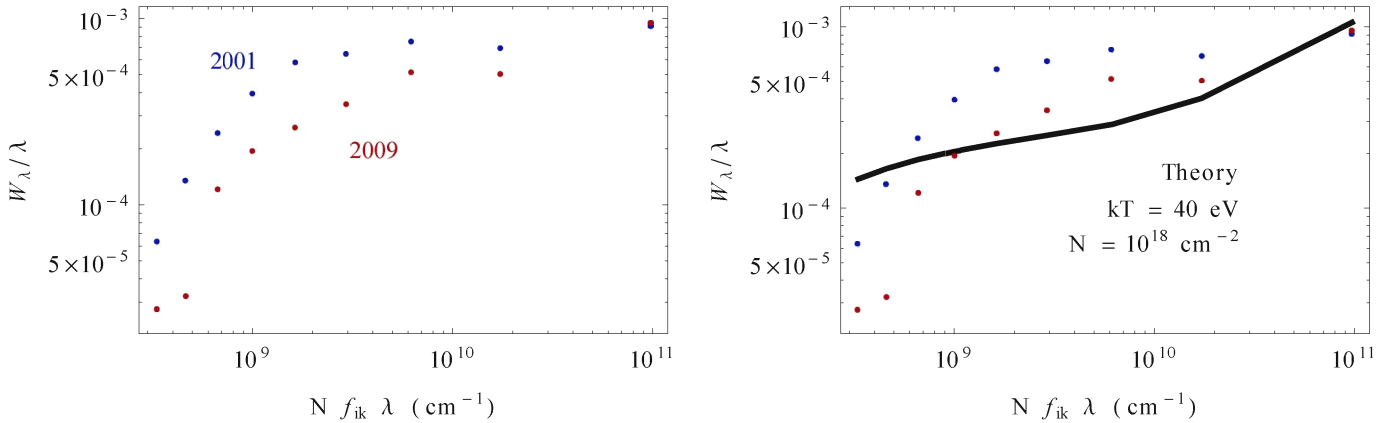
4.2 Comparing Experimental and Theoretical COG

Using the equivalent widths in Tables 4.1 and 4.2, experimental COGs have been plotted in Figure 4.2(a) for the Ne IX lines in the 2001 and 2009 data.

The data appear promising for a curve of growth analysis; both the 2001 and 2009 equivalent widths exhibit the classic COG shape seen in Figure 3.8. The high n transitions (on the left side of the plot) exhibit the linear behavior expected for unsaturated lines in a curve of growth, and the log and square root components seem to be present too.

The vertical offset between the two sets of data is odd, since neither a temperature change nor a column density change can account for such a shift (varying N and kT will be discussed shortly). Since the equivalent width measurements described in Section 4.1 are unlikely to be off by the factor of 3 or 4 for the high signal to noise $n = 5, 6$ lines, the offset is unlikely to be an error in equivalent width measurement. The offset could be due to an extra line broadening mechanism at work in the 2001 data but not in the 2009 data; broader lines would increase the equivalent width for every line in the spectrum, explaining the systematic offset. However, it is unlikely that a new type of broadening is at work in one plasma and not the other, given that there is no difference in the experimental setup between the two. It is also possible that a difference in the post processing of the data or even an unexpected leak in the gas cell created the disparity. Data from other experiments is currently being analyzed in order to further investigate this disparity.

Using a Voigt profile to generate theoretical line widths for a plasma of temperature $kT = 40$ eV and column density $N = 10^{18}$ cm^{-2} yields the curve shown in Figure 4.2(b). This column density is the column density of Ne IX. As discussed in section 1.4 the column density of neon in the gas cell is set to be 10^{18} cm^{-2} , so this value of N assumes that all of the neon is Ne IX. In Section 2.2 it is shown that PrismSPECT predicts that 85% of the neon is Ne IX, so 10^{18} cm^{-2} is likely to be the right order of magnitude. The temperature was chosen as 40 eV because that temperature produces satisfactory results in PrismSPECT, and simulations and more detailed radiation hydrodynamic studies have predicted this temperature [19]. While the curve of growth method should be able to



(a) Experimental COG for the 2001 and 2009 data using the Ne IX lines $1s^2 \rightarrow 1snp$. Each separate x-value represents a Ne IX absorption line from the spectrum, and each line has an equivalent width listed for the 2001 data and the 2009 data. The $1s^2 \rightarrow 1s2p$ transition is the right most point, and the transitions progress in order to the left, so the leftmost transition is $1s^2 \rightarrow 1s10p$. Low signal to noise for the higher n transitions makes it difficult to accurately measure the equivalent width, so the $n = 9, 10$ transitions points have large errors.

(b) Identical to Figure 4.2(a), only now a theoretical COG has been added. The theoretical COG (black) is derived using the Voigt profile as the line-profile function and $N = 0.85 \times 10^{18} \text{ cm}^{-2}$, $kT = 40 \text{ eV}$. The theoretical curve is a series nine points just like the experimental data; the points are connected to differentiate theory from experiment.

Figure 4.2: Curves of growth for the Ne IX lines in the 2001 and 2009 spectra.

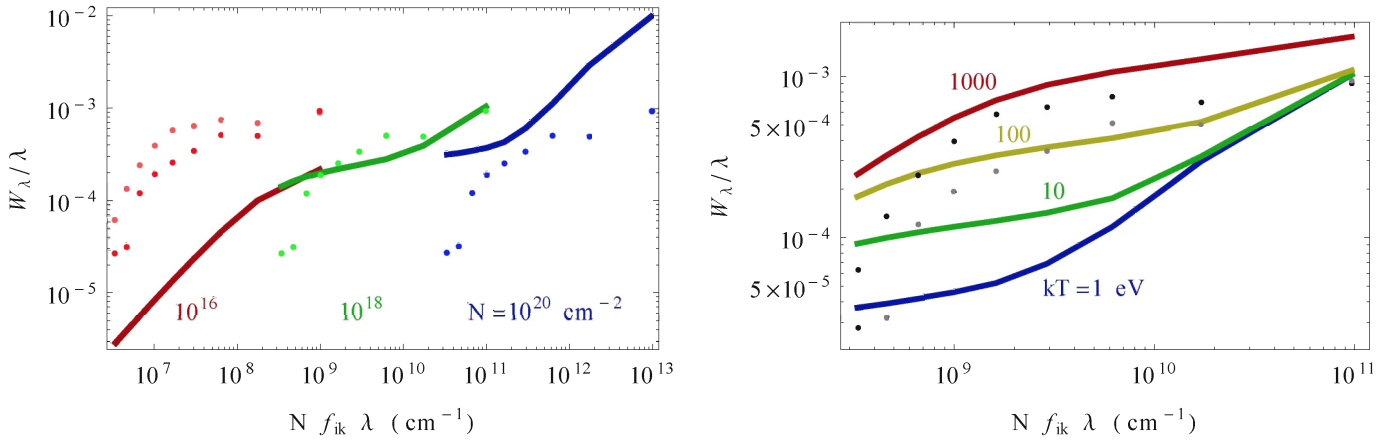
predict the values of N and kT itself, it is important to start at values where the theoretical COG is expected to be close to the experimental COG.

The theoretical COG does not match either data set in shape and is far from the 2001 data in magnitude. In fact, the theoretical curve predicts that all lines are in the log and square root portion of the curve of growth which would imply all of the theoretical lines are saturated. The data show a different trend. The higher n transitions appear to be on the linear part of the curve of growth, and the lower n transitions exhibit log and square-root behavior.

This discrepancy may be addressed within the framework of the Voigt profile by adjusting the parameters N and kT . In Figure 4.3, both N and kT are varied in a theoretical spectrum. The 2001 and 2009 data are also included for reference.

Figure 4.3(a) shows how the COG changes with changing N . A significant decrease (down to $N = 10^{16} \text{ cm}^{-2}$) shrinks the optical depth in all theoretical lines enough to put most lines on the linear regime, matching the shape of the experimental lines. An increase in N , while impossible since the column density of an ion cannot exceed the column density of the atom, has the opposite effect.

Figure 4.3(b) shows how the COG changes when kT is changed. The temperature controls the Doppler width ($\delta \propto \sqrt{kT}$) and contributes by convolution to the Voigt profile width, so increasing kT increases the line-profile width. An increasing line width desaturates a saturated line core by distributing the absorption cross section more broadly. This broadening process increases W_λ for all saturated lines, especially the Gaussian-dominated saturated lines (the log region of the COG). The increasing the line widths also delays the onset of the log and square root portions of the COG.



- (a) The effect of varying N on the COG is shown. N is set to three different values, 10^{16} , 10^{18} , and 10^{20} cm^{-2} , while kT is fixed at 40 eV. Theoretical COGs (solid, dark) are generated in each case, to be compared with the 2001 (light) and 2009 (medium) data. A decrease in N brings a significant amount of the COG in to the linear regime, while an increase in N brings most of the COG in to the square root regime. In each case the experimental data slides along the x-axis since N is part of the independent variable.
- (b) The effect of varying kT in the COG is shown. For N fixed at 10^{18} cm^{-2} , kT is shown at four different values: 1, 10, 10^2 and 10^3 eV. An increase in kT increases W_λ for every line, shifting the COG upward. The experimental data (2001 in black and 2009 in gray) is not shifted in any way by a change in kT .

Figure 4.3: The effect of varying N and kT on the theoretical COG.

The 1000 eV curve (red), for example, shows a few lines on the linear part of the COG, while the 1 eV curve (blue) only exhibits the log and square root parts.

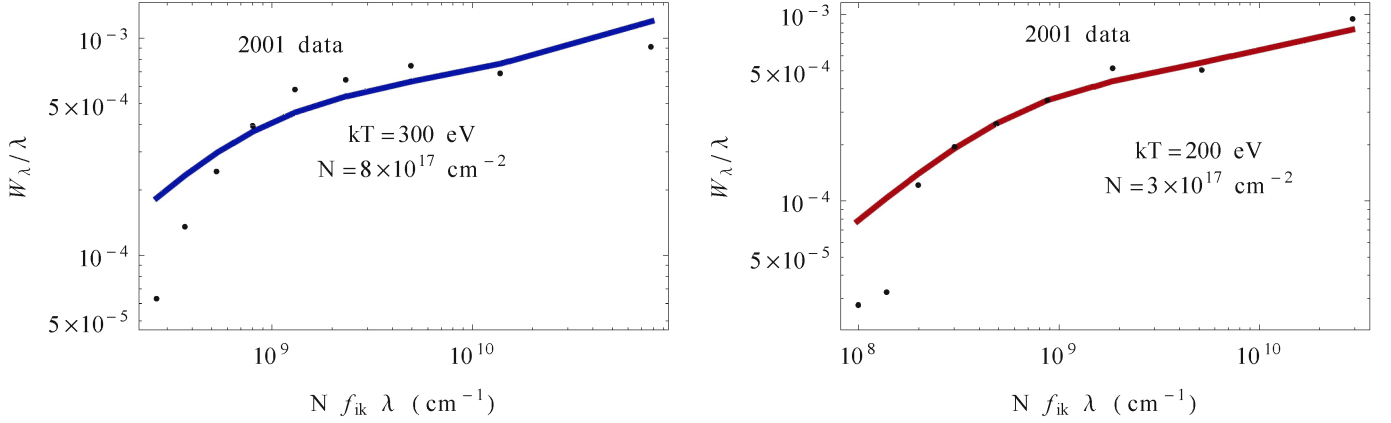
To find an acceptable fit to the data, N and kT need to be changed from the intuitive values used in Figure 4.2(b). To fix the shape of the theoretical COG, N must be lowered for the inclusion of the linear regime. Since that will lower the theoretical COG even farther, kT needs to be increased to bring the theoretical equivalent widths up to the data. The best fit parameters needed to fit both data sets are shown in Figure 4.5. The best fit column densities (8×10^{17} and $3 \times 10^{17} \text{ cm}^{-2}$ for the 2001 and 2009 data) are reasonable results. The 2001 column density is very close to the PrismSPECT prediction of 8.5×10^{17} .

The best fit temperatures, on the other hand, are too large. The 2001 and 2009 best fit temperatures, $kT = 300$ eV and 200 eV respectively, would result in a collisionally ionized (and therefore not predominantly photoionized) plasma. Neither temperature is near to the ~ 40 eV temperatures predicted by radiation hydrodynamic studies of the neon in the gas cell [19].

The temperatures need to be high in the theoretical curve of growth to increase W_λ for all lines through line-profile broadening. Since a practical limit has been placed on the temperature, another significant line broadening mechanism must be important.

Stark broadening due to the electric microfield around an absorbing ion, already introduced in Section 3.3.5, could be another important line broadening mechanism. Including Stark broadening in a detailed COG analysis is the subject of current research, so a preliminary analysis is presented here.

To see how Stark broadening may change the COG analysis, it is approximated it as a Lorentzian



(a) The best fit theoretical COG for the 2001 data requires $N = 8 \times 10^{17}$ cm $^{-2}$ and $kT = 300$ eV. (b) The best fit theoretical COG for the 2009 data requires $N = 3 \times 10^{17}$ cm $^{-2}$ and $kT = 200$ eV.

Figure 4.4: Best fit theoretical COGs for the 2001 and 2009 data.

broadening effect. The Stark profiles shown in Figure 3.6 are certainly not Lorentzian, but they do have Lorentzian-like wings. However, it is still common in spectroscopy to treat Stark broadening as Lorentzian [22].

As discussed in Section 3.3.5, the Stark broadening may be included by convolution with the other broadening mechanisms. Conveniently, the convolution of two Lorentzian profiles with parameters $\gamma_{natural}$ and γ_{Stark} is again Lorentzian² with parameter $\gamma_{new} = \gamma_{natural} + \gamma_{Stark}$. The Voigt profile can still be used in this analysis, only with γ replaced by γ_{new} .

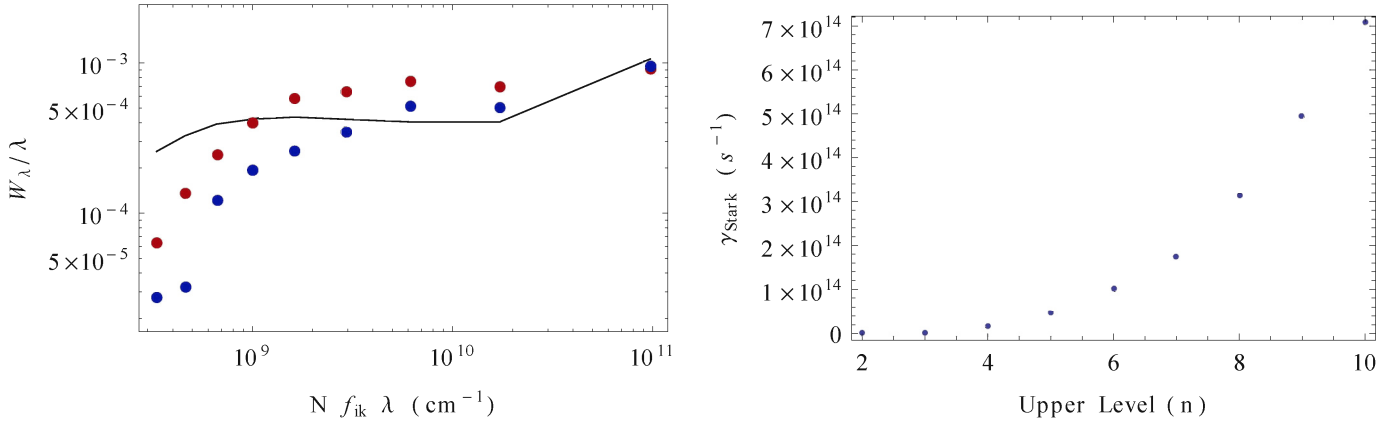
Estimates for the values for γ_{Stark} were obtained from [31]. A curve of growth including γ_{new} in the place of γ is shown in Figure 4.5(a), where N and kT are again set to 10^{18} cm $^{-2}$ and 40 eV.

Stark broadening aids in the COG analysis by broadening the theoretical line profiles without the need for additional Doppler broadening introduced by an increase in temperature.

However, the increased widths due to Stark broadening is most prevalent in the high n transitions, increasing the equivalent width of the Stark broadened COG beyond both the 2001 and 2009 data. The lack of additional broadening in the low n transitions leaves the Stark COG below the 2001 and 2009 data for the $n = 3, 4$ transitions near the right of Figure 4.5(a). The lack of broadening in these low n transitions and the increased broadening seen in higher n transitions could be responsible for the flat (in fact, there is a minor decrease in W_λ from the 4 to 3 transition, behavior not explained by the classic curve of growth) trend in both data sets in that region.

This investigation into Stark broadening is only preliminary; Stark broadening was approximated as Lorentzian and the widths were taken from an outside source [31]. Using Equation (3.39) to accurately assess the effect of Stark broadening is the subject of ongoing research.

²This result is conditional on the independence of the two distributions. Convolutions are also commutative and associative, so the order of convolution for any number of distributions doesn't matter.



(a) A theoretical curve of growth accounting for Stark broadening. Stark broadening is approximated as Lorentzian. N and kT are 10^{18} cm^{-2} and 40 eV . (b) The Stark widths, in frequency, from [31]. Stark widths increase rapidly with n , the principal quantum level of the upper level.

Figure 4.5: Preliminary Stark broadened COG analysis.

4.3 Conclusion

The gas cell experiment at the Z facility in Sandia National Laboratory is a large collaboration with an ambitious goal: to produce an astrophysically relevant photoionized plasma in the laboratory. A well characterized laboratory plasma can be used to benchmark codes astrophysicists rely on, a check that has been out of reach until recently for photoionized plasma codes.

A curve of growth analysis was applied to the strongest series of lines in the neon absorption spectrum (the Ne IX $1s^2 \rightarrow 1snp$ transitions) from two separate gas cell experiments. The goal of this analysis was to calculate the column density of Ne IX to learn about the charge state distribution in the plasma.

Though the Ne IX ionic column density of $8 \times 10^{17} \text{ cm}^{-2}$ derived for the 2001 data agrees well with PrismSPECT simulations of the plasma conditions, uncertainty in the line broadening mechanisms doesn't allow for full confidence in this result.

Including Stark broadening in the curve of growth spectral analysis is the focus of an ongoing investigation; in the near future more accurate estimations of the ionic column density of Ne IX in the gas cell will be available.

When the line broadening mechanisms have been completely identified, an accurate ion balance will be inferable from the measurement of ion column densities. This ion balance will supply a model independent way to test the accuracy of astrophysical photoionization codes and better understand astrophysical data.

Chapter 5

Acknowledgements

I would like to thank The Charles Price Summer Research Fellowship, from the Provost's Office of Swarthmore College, for supporting my research. There are several people whose guidance has been indispensable to me. Jim Bailey from Sandia National Laboratory offered helpful advice on my curve of growth analysis and supplied the spectrometer data. Roberto Mancini at the University of Nevada first suggested that Stark broadening could be a factor in my analysis. Michael Rosenberg, a former student researcher, supplied the VISRAD workspace used in Chapter 2. Eric Jensen offered insightful comments on earlier versions of this document. My research advisor, David Cohen, has provided thoughtful guidance and essential feedback on my work. I would like to thank him for introducing me to this exciting research.

Bibliography

- [1] P. van Hoof, Atomic line list v2.05b12, <http://www.pa.uky.edu/~peter/newpage/>, 2009.
- [2] R. K. Smith, N. S. Brickhouse, D. A. Liedahl, and J. C. Raymond, *ApJ*, **556**, L91 (2001).
- [3] G. Del Zanna and H. E. Mason, *A&A*, **433**, 731 (2005).
- [4] G. B. Rybicki and A. P. Lightman, *Radiative processes in astrophysics*, Wiley-Interscience, 1979.
- [5] J. E. Dyson and D. A. Williams, *The physics of the interstellar medium*, 1997.
- [6] D. E. Osterbrock and G. J. Ferland, *Astrophysics of gaseous nebulae and active galactic nuclei*, 2006.
- [7] S. Watanabe et al., *ApJ*, **651**, 421 (2006).
- [8] R. R. J. Antonucci and J. S. Miller, *ApJ***297**, 621 (1985).
- [9] A. C. Brinkman et al., *Astronomy and Astrophysics* **396**, 761 (2002).
- [10] A. Kinkhabwala et al., *ApJ*, **575**, 732 (2002).
- [11] J. S. Kaastra et al., *A&A*, **386**, 427 (2002).
- [12] C. J. Hess, S. M. Kahn, and F. B. S. Paerels, *ApJ*, **478**, 94 (1997).
- [13] J. E. Bailey et al., Neon Photoionization Experiments Driven By Z-Pinch Radiation, in *Bulletin of the American Astronomical Society*, volume 32 of *Bulletin of the American Astronomical Society*, page 1215, 2000.
- [14] C. F. McKee, The Multiphase Interstellar Medium, in *The Physics of the Interstellar Medium and Intergalactic Medium*, edited by A. Ferrara, C. F. McKee, C. Heiles, & P. R. Shapiro, volume 80 of *Astronomical Society of the Pacific Conference Series*, pages 292–+, 1995.
- [15] R. B. Spielman et al., *Physics of Plasmas* **5**, 2105 (1998).
- [16] J. Macfarlane, I. Golovkin, P. Woodruff, and P. Wang, *APS Meeting Abstracts* , 1181 (2003).
- [17] M. J. Rosenberg, *Spectral and Hydrodynamic Modeling of X-Ray Photoionization Experiments*, 2008.

- [18] J. J. MacFarlane, *Journal of Quantitative Spectroscopy and Radiative Transfer* **81**, 287 (2003), Radiative Properties of Hot Dense Matter.
- [19] I. M. Hall et al., *Ap&SS*, **322**, 117 (2009).
- [20] L. Spitzer, *Physical processes in the interstellar medium*, 1978.
- [21] D. J. Griffiths, *Introduction to Electrodynamics*, Addison Wesley, third edition, 1999.
- [22] H. R. Griem, *Principles of Plasma Spectroscopy*, Cambridge University Press, 1997.
- [23] D. Schroeder, *An Introduction to Thermal Physics*, Addison Wesley Longman, 1999.
- [24] W. Thompson, *Computers in Physics* **7**, 627 (1993).
- [25] R. Wells, *Journal of Quantitative Spectroscopy and Radiative Transfer* **62**, 29 (1999).
- [26] N. Zettili, *Quantum Mechanics: Concepts and Applications*, Wiley, 2 edition, 2009.
- [27] C. A. Iglesias, H. E. Dewitt, J. L. Lebowitz, D. MacGowan, and W. B. Hubbard, *Phys. Rev. A*, **31**, 1698 (1985).
- [28] C. F. Hooper and R. C. Mancini, *Physica Scripta* **1993**, 65 (1993).
- [29] L. A. Woltz and C. F. Hooper, *Phys. Rev. A* **38**, 4766 (1988).
- [30] R. Mancini, personal communication, 2010.
- [31] R. Mancini, Photoionized plasmas at z relevant for astrophysics, High-Power Lasers and Pulsed Power Workshop Lecture, 2009.